

Height Estimation and Control of Rotorcraft in Ground Effect

Using Spatially Distributed Pressure Sensing

Chin Gian Hooi

Software Engineer, Commercial Navigation Systems

Rockwell Collins, Melbourne FL

Francis D. Lagor

Graduate Research Assistant, Department of Aerospace Engineering

University of Maryland, College Park MD

Derek A. Paley

Willis H. Young Jr. Associate Professor of Aerospace Engineering Education

Department of Aerospace Engineering and Institute for Systems Research

University of Maryland, College Park MD

Abstract

This paper describes a dynamic height controller for rotorcraft hovering and landing in ground effect based on flowfield sensing and estimation. The rotor downwash in ground effect is represented using a ring-source potential-flow model selected for real-time use and validated experimentally. A nonlinear dynamic model of the heave test stand that represents the dynamics of a rotorcraft in ground effect is presented. Flowfield pressure measurements are compared with flow-model predictions in a grid-based recursive Bayesian filter to estimate height above ground. Height control in ground effect using the estimated height is implemented with a dynamic linear controller. The experimental results show that height estimation and control are possible for a miniature autonomous rotorcraft by comparing two sets of differential pressure measurements in the rotor downwash with a low-order

Portions of this work were presented at the IEEE Aerospace Conference, Big Sky, MT, March 7–14, 2015 and at the 71st Annual Forum of the AHS, Virginia Beach, VA, May 5–7, 2015.

aerodynamic model in a Bayesian filter.

Nomenclature

$(\dot{\cdot}), (\ddot{\cdot})$ First- and second-order time derivative operators

$(\cdot)^*$ Superscript to denote equilibrium condition

$(\hat{\cdot})$ Designation to denote estimated quantity

α Low-pass filter gain, $0 < \alpha < 1$

δ Gain for quadratic smoothing optimal trade-off curve, $\delta > 0$

η Measurement noise (m/s)

θ Test stand angle (rad)

ν_1 Rotorcraft in ground effect control input

ν_2 Test stand control input

ν_{FW} Feed-forward control input

ν_{PI} Proportional-integral feedback control input

$\rho_1, \rho_2, \bar{\rho}_1, \bar{\rho}_2$ Composite variables in the ring-source model

σ_m, σ_p Measurement and process noise standard deviations

ϕ Velocity potential

Λ Quadratic smoothing function

a Calibration constant to convert differential pressure to velocity ($\text{m}^2 \text{s/kg}$)

b_1, b_2 Test stand and aerodynamic damping coefficients ($\text{kg m}^2/\text{rad/s}$, kg/s)

c Scaling factor for unit integral of posterior over the state space

$\hat{e}_x, \hat{e}_y, \hat{e}_z$ Unit vectors in the test stand x, y, z-directions

$f_1(\cdot), f_2(\cdot)$ General functions

g Gravitational acceleration (m/s^2)

h Height above ground plane (m)

h_O Angular momentum about point O ($\text{kg m}^2 \text{rad/s}$)

l_1 Distance from point O to center of mass G (m)

- l_2 Distance from point O to counterweight M_2 (m)
- m Rotorcraft mass (kg)
- p Probability density
- r Radial location of query point (m)
- s Source strength (m^2/s)
- s_{max} Maximum source strength of ring-source potential flow model (m^2/s)
- $t, \Delta t$ Time and time step interval (s)
- v Radial velocity component (m/s)
- v_i Induced velocity (m/s)
- w Vertical velocity component (m/s)
- x, y, z Coordinates of query point in rotor body frame (m)
- z_1, z_2 Components of state vector Z : height, vertical velocity (m,m/s)
- A State dynamics matrix
- B Control matrix
- D Bidiagonal matrix for quadratic smoothing
- $E(\cdot)$ Complete elliptic integral of the second kind
- G Center of mass location
- I Identity matrix of suitable dimension
- I_O Moment of inertia about point O (kg m^2)
- J Moving-average filter data points
- K_1, K_2 Control gains
- K_P, K_I Proportional and integral control gains
- $K(\cdot)$ Complete elliptic integral of the first kind
- L Set of sensor measurements
- L_0 Set of prior sensor measurements
- L_1 Distance from point O to rotor mass m (m)
- L_2 Distance from point O to ground plane (m)
- M_1, M_2 Pendulum setup total mass, counterweight mass (kg)

N Number of ring sources

O Test stand pivot point

\tilde{P}_j Differential pressure sensor measurement j (Pa)

R Rotor radius (m)

\mathbb{R} Set of real numbers

T, T_{IGE} Thrust out of ground effect, thrust in ground effect (N)

V Flow velocity (m/s)

\tilde{V} Flow velocity measurement (m/s)

Z State vector

Subscripts

k Ring source index

l Sensor location index

m Number of sensors

p Current iteration

Introduction

Rotorcraft operation in ground effect (IGE) presents substantial challenges for vehicle control, including landing with low-impact velocity and maintaining near-ground hover in low-visibility conditions such as brownout [1], fog [2], precipitation, or darkness. Safe IGE operation in a degraded visual environment may require non-traditional sensors and a controller capable of handling uncertainty. Previous authors have developed landing controllers based on robust or adaptive control techniques. For example, Serra and Cunha [3] adopt an affine parameter-dependent model that describes the linearized error dynamics for a predefined landing region and implements H_2 feedback control. Mahony and Hamel [4] develop a parametric adaptive controller that estimates the helicopter aerodynamics onboard and modulates the motor torque, rather than the collective pitch, during takeoff and landing. Nonaka and Sugizaki [5] implement ground-effect compensation and integral sliding-mode control to suppress the modeling error of the vehicle dynamics in ground effect. Hu et al. [6] estimate the height of a quadcopter relative to an oscillat-

ing platform using an onboard camera, generate a time optimal reference trajectory, and land the vehicle using an adaptive robust controller that adapts to the changes in thrust due to ground effect. These control techniques often require a system model with empirically fit aerodynamic coefficients that are unique to each vehicle.

Safe IGE operation also requires accurate estimation of the proximity and relative orientation of the ground plane. Height-estimation methods currently exist for micro aerial vehicles (MAVs) based on ultrasonic, barometric pressure or optical sensors. However, ultrasonic sensors work only for proximity sensing and are not well suited for an angled or irregular ground plane [7]. Barometric pressure sensors typically work well for large height differentials [8], but atmospheric pressure fluctuations result in sensor drift and local pressure variations IGE cause the divergence of height estimate. Likewise, the effectiveness of vision-based sensors is limited in degraded visual environments and the vision algorithms typically require extensive computational resources. This work shows that flow-sensing of the ground effect with differential pressure probes is a useful sensing modality for height estimation. We demonstrate this claim in experiments with a flat, horizontal ground plane.

Previous authors have quantified ground effect empirically or through the use of an underlying aerodynamic model. Lee et al. [9] present particle-image-velocimetry results to examine the wake of a small rotor, a few inches in radius, with blade-tip vortices interacting with a horizontal ground plane. Tanner et al. [10] present comprehensive measurements of rotor outwash IGE at varying rotor heights and thrust conditions, including rotor outwash velocities and directions, rotor loads, fuselage loads, and ground pressures. Nonaka and Sugizaki [5] take an empirical approach to measuring the ground effect on rotor thrust as a function of motor voltage. Mahony and Hamel [4] use an approximation of the down-flow velocity ratio based on a piecewise linear approximation of Prouty [11] to estimate rotor-thrust variation IGE. Higher-fidelity analytical models include Govindarajan's [12] free-vortex modeling to accurately predict the nature of the rotor-wake vortices. Kalra [13] uses a Reynolds-Averaged Navier-Stokes (RANS) based computational fluid dynamics (CFD) framework to model the unsteady rotor wake IGE, which includes tip vortex and rotor ground wake formation, turbulence and viscous wall effects at the ground, and the effect of rotor tip shapes.

Cheeseman and Bennett [14] provide a classic analytical model for ground effect, which we adapt for

this work, based on aerodynamic modeling using the method of images. Knight and Hefner [15] and Rossow [16] used a similar approach by representing the rotor wake IGE as a vortex cylinder. The Knight and Hefner ground effect model is derived from a cylindrical circulation sheet and an image cylinder to create a ground plane. The flow velocity equations were derived for a point in the plane of the rotor, which is not immediately useful here because it is only applicable in the plane of the rotor. Furthermore, there is no diffusion of the circulation cylinder outward as it impinges on the the ground plane, i.e., it has constant diameter. Knight and Hefner were primarily interested in the induced velocity in the axial direction at the plane of the rotor for thrust calculations, whereas we are interested in the flowfield within the volume just beneath the rotor, including both the axial and radial flow components. The use of an idealized aerodynamic model permits comparison to measurements from sensors such as differential-pressure airspeed sensors [17]. Lagor et al. [18] and DeVries et al. [19] have previously shown that a reduced-order flow model may be rapidly evaluated within a recursive filter to perform estimation and control tasks in an uncertain flow environment, albeit in an underwater setting.

Our previous paper [20] developed the theoretical framework for dynamic feedback control in hover and landing IGE based on a potential flow model. We replaced the point-source model of Cheeseman and Bennett [14] with multiple ring sources; the mirror images create a ground plane. The reduced-order model relates the flowfield velocities to height IGE; it is capable of sufficiently fast evaluation for control purposes. A nonlinear dynamic model of rotorcraft landing IGE was presented, assuming a rigid rotor commonly found in MAV rotorcraft [21]. Height estimation of rotorcraft IGE using spatially distributed airspeed measurements was accomplished in simulation with a grid-based recursive Bayesian filter. The Bayesian framework is capable of fusing data from multiple sensing modalities and multiple sensors. The observer-based feedback controller was implemented in simulation to illustrate the theoretical results.

Our previous paper [22] outlined an improved ring-source potential flow model consistent with experimental observations. We derived a nonlinear dynamic model of a heave test stand that represents the dynamics of a rotorcraft IGE. Experimental results for the open-loop dynamics were presented. We also presented experimental validation of the flow modeling and estimation framework at a static height.

This paper uses reduced-order flow modeling to model and control the rotor height IGE. Flow-velocity components are measured using multi-component differential pressure probes [17] and compared with

the mean-field flow model in a grid-based recursive Bayesian filter to estimate rotorcraft height. We expand on the previous work by validating the flow model at suitable probe locations for the entire operational region. Specifically, the contributions of this paper are as follows: (1) a model-based, closed-loop feedback controller that drives a rotorcraft to a commanded height in ground effect using spatially distributed differential-pressure measurements; (2) experimental validation of the flow model on a miniature autonomous rotorcraft with recommended probe placement for the best performance in the operational region of ground effect; and (3) experimental validation of the flow-sensing and height-control framework on a miniature rotorcraft test stand.

This paper shows that the framework presented is capable of estimating and tracking rotor height IGE by comparing multiple differential-pressure sensor measurements to a flow model using a Bayesian filter. The proposed framework assumes that the flowfield is well-approximated by a quasi-static potential flow model presented below and the rotorcraft is within one rotor diameter of a flat and horizontal ground plane. Under these assumptions, experimental results on a MAV-scale rigid rotor show height estimation is accurate to within 5% mean error and height tracking is accurate to within 9% mean error.

Flow Modeling

Many previous attempts at modeling the flowfield of a rotor IGE have been made, as detailed above. Our motivation is to develop a flow model that can be recursively evaluated in real-time within a control loop, which has not been previously accomplished. Another goal is to develop estimation algorithms and control laws that are computationally efficient, i.e., they can be evaluated in real-time at a sufficiently high rate with minimal computational requirements. This framework is useful for low- or no-visibility altitude estimation in ground effect using flow sensors (alone, or in conjunction with other sensing modalities), with applications including autonomous shipboard landing.

Let R denote the rotor radius, v_i the rotor induced velocity, and h the rotor height. Cheeseman and Bennett [14] model the rotor downwash impinging on the ground plane by representing the rotor as a three-dimensional point source with strength $s = R^2 v_i / 4$ and the ground plane as a mirror-image source to enforce no flow through the ground plane, as shown in Fig. 1. The sources are separated by a distance

2*h*. The velocity potential for the location (x, y, z) in the flowfield is [14]

$$\phi = -\frac{s}{\sqrt{x^2 + y^2 + (z - h)^2}} - \frac{s}{\sqrt{x^2 + y^2 + (z + h)^2}}. \quad (1)$$

Taking the gradient of the velocity potential yields the flow velocity components [14].

The Cheeseman and Bennett [14] flow model has been shown experimentally to capture the aggregate relationship between rotor thrust IGE and rotor height. However, it represents the spatial flowfield of a rotor IGE with insufficient accuracy for our purposes, because we require the model to be more representative of the real flow at various query points throughout the flowfield for comparison to our sensor measurements during real-time operation. Figure 1 shows the flow vectors just below the rotor plane extend radially outward, as opposed to downward. Since the rotor is modeled as a point source, the strongest vectors are at the hub and diffuse in strength radially outward. We replace the single point source of Cheeseman and Bennett [14] with multiple ring sources to create a more uniform spatial distribution of the flowfield sources.

As shown in Fig. 2, the rotor is modeled by N ring sources and the ground plane is modeled by their mirror images to enforce no flow through the ground plane. Note that ring $k = 1$ is at the rotor tip and the ring indices increase radially inward with equal radial spacing of R/N . The radial location of each ring k is

$$r_k = R - (k - 1)\frac{R}{N}. \quad (2)$$

Similar to the inflow ratio distribution of a rotor [23], the strength s_k of ring k varies with radial location according to

$$s_k = \frac{s_{max}}{R}r_k, \quad (3)$$

where the maximum source strength s_{max} is located at the rotor tip $r_1 = R$. We choose the source strengths according to the total volumetric flow through the rotor disk, similar to Cheeseman and Bennett [14]. Although ring sources emanate in all directions, only the bottom half of the emanation is included as the rotor flow. Additionally, the outermost ring source, which is the strongest, has only a quarter of its emanation considered because the emanation outwards and upwards does not contribute to the rotor flow.

Let πR^2 denote the rotor disk area. The strength s_k of ring source k represents the volumetric flow rate per unit length. The total flow rate satisfies

$$\frac{1}{2} \sum_{k=1}^N 2\pi r_k s_k - \frac{1}{4} (2\pi R s_{max}) = \pi R^2 v_i. \quad (4)$$

From arithmetic series and sum of a sequence of squares, we have

$$\sum_{k=1}^N k = \frac{N(N+1)}{2} \quad \text{and} \quad \sum_{k=1}^N k^2 = \frac{N(N+1)(2N+1)}{6}. \quad (5)$$

Substituting Eqns. (2), (3), and (5) into Eqn. (4) yields

$$s_{max} = \frac{6NRv_i}{2N^2 + 1}. \quad (6)$$

The velocity potential of ring source k is [24]

$$\phi_k(r, r_k, z) = \frac{-s_k r_k K(M)}{\pi \sqrt{\rho_1(r, r_k, z)}}, \quad (7)$$

where $\rho_1 = (r + r_k)^2 + z^2$, r and z are the radial location and elevation of the query point in the rotor reference frame (positive down), respectively, $K(M)$ is the complete elliptic integral of the first kind, and $M = 4rr_k/\rho_1$. The radial $v_k(\rho_1, \rho_2)$ and vertical $w_k(\rho_1, \rho_2)$ velocity components of ring source k are [24]

$$v_k = \frac{r_k s_k}{2\pi r \sqrt{\rho_1}} \left[K(M) + \frac{r^2 - r_k^2 - z^2}{\rho_2} E(M) \right], \quad (8)$$

$$w_k = \frac{-s_k r_k z E(M)}{\pi \rho_2 \sqrt{\rho_1}}, \quad (9)$$

where $\rho_2 = (r - r_k)^2 + z^2$ and $E(M)$ is the complete elliptic integral of the second kind.* The velocity components of the flowfield are the sum of each ring source and their image ring-source contributions, i.e.,

$$v(r, z) = \sum_{k=1}^N v_k(\rho_1, \rho_2) + \sum_{k=1}^N v_k(\bar{\rho}_1, \bar{\rho}_2), \quad (10)$$

$$w(r, z) = \sum_{k=1}^N w_k(\rho_1, \rho_2) + \sum_{k=1}^N w_k(\bar{\rho}_1, \bar{\rho}_2), \quad (11)$$

* $K(M)$ and $E(M)$ are evaluated using the `elliptic` function in MATLAB.

where $\bar{\rho}_1 = (r + r_k)^2 + (2h - z)^2$ and $\bar{\rho}_2 = (r - r_k)^2 + (2h - z)^2$. Note that the ring-source potential flow model takes rotor induced velocity v_i , probe radial r , and vertical z locations as inputs.

Figure 3 shows the flowfield generated by the ring-source potential flow, with streamlines and speed distribution shown for various heights. Speed is denoted by $\|V\| = \sqrt{v^2 + w^2}$. The variations in speed distribution with height serve as an informative tool for the placement of sensors to measure the flowfield experimentally. The potential flow model is qualitatively similar to the flow visualization below a rotor IGE by Lee et al. [9]. As the flow moves down from the rotor plane, it decelerates to zero flow velocity at the stagnation point where the rotor centerline intersects the ground plane. Moving radially outward, the flow deceleration region is easiest to distinguish for $h = 1.0R$ in Fig. 3. In contrast, the flow acceleration region is where the streamlines change direction from downward to radially outward. As the rotor approaches the ground, the streamlines are compressed, which is best illustrated for $h = 0.5R$ in Fig. 3. Evidently, the flow speed is the highest in the flow acceleration region for $h = 0.5R$, as opposed to $h = 2.0R$, since the flow is compressed more with less space between the rotor plane and the ground. This effect is analogous to moving a water jet (the rotor) closer to a wall (the ground plane), since the jet speed in the flow acceleration region is highest when it is close to the wall.

Although the rotor downwash IGE as visualized in the work of Lee et al. [9] is not laminar, we model it using potential flow theory and mitigate unmodeled effects by using a sensor model with uncertainty. Equations (8) and (9) model the mean velocity of the dominant flow; the unmodeled effects, such as turbulence and blade tip vortices, are fluctuations away from the mean. Flow-velocity components \tilde{V} are measured below the rotor in the experimental setup using differential pressure probes [17] (measurement \tilde{V} corresponds to either the radial \tilde{v} or the vertical \tilde{w} velocity component). We assume the velocity component V is corrupted by zero-mean Gaussian white noise η with standard deviation σ_m , resulting in the measurement model

$$\tilde{V} = V + \eta. \quad (12)$$

Dynamics of the Test Stand

Figure 4(a) shows the compound-pendulum heave test stand used to verify the flow model, rotor IGE dynamics, and closed-loop control. The test stand is constructed as a four-bar linkage, so that the rotor is nearly always parallel to the ground plane with one degree of freedom in the heave direction. This setup allows the use of journal bearings, which are smoother than linear carriages and rails in a vertical configuration. This setup also has the added benefit of allowing a counterweight to balance the system weight and to reduce the motor load. Figure 4(b) shows the free-body diagram of the compound pendulum. The lateral displacement is minimized by mounting the setup at the midstroke, i.e., at a height of $1.25R$.

The angular momentum of the compound pendulum is

$$h_O \hat{e}_x = I_O \dot{\theta} \hat{e}_x, \quad (13)$$

where I_O is the moment of inertia about point O , θ is the angle increasing counter-clockwise from down and $\dot{\theta}$ is the angular velocity. The time derivative of the angular momentum h_o equals the moment about O . The dynamics in the \hat{e}_x direction are

$$I_O \ddot{\theta} = L_1 T_{IGE} \sin \theta - l_1 g \sin \theta (m + M_1) + l_2 M_2 g \sin \theta - b_1 \dot{\theta}, \quad (14)$$

where $\ddot{\theta}$ is the angular acceleration, l_1 is the distance from O to the center of mass G , l_2 is the distance from O to counterweight M_2 , L_1 is the distance from O to rotor mass m , M_1 is the total mass of the pendulum setup, b_1 is the damping coefficient due to aerodynamics and/or friction, and g is the gravitational acceleration. The parameters for the experimental setup are $l_1 = 0.2921$ m (11.15 in), $l_2 = 0.4572$ m (18 in), $L_1 = 0.9398$ m (37 in), $m = 0.35$ kg (0.7714 lb), $M_1 = 0.304$ kg (0.6702 lb), and $M_2 = 0.34$ kg (0.7496 lb).

The rotor thrust T_{IGE} is the total thrust experienced by the rotor in the presence of a ground plane. The Cheeseman and Bennett model is used to relate T_{IGE} and height h in hover for $0.5 \geq h/R \geq 2.0$, i.e., [14], [23]

$$T_{IGE} = \frac{1}{1 - \frac{R^2}{16h^2}} T = \frac{16h^2}{16h^2 - R^2} T. \quad (15)$$

The rotor thrust T is the total thrust experienced by the rotor if the ground plane were not present and power Tv_i were held constant [14].

In terms of the height $h = L_2 - L_1 \cos \theta$, where L_2 is the distance from point O to the ground plane, we have the vertical velocity and acceleration as

$$\dot{h} = L_1 \dot{\theta} \sin \theta, \quad (16)$$

$$\ddot{h} = L_1 \dot{\theta}^2 \cos \theta + L_1 \ddot{\theta} \sin \theta. \quad (17)$$

Since the compound pendulum is mounted at midstroke, we approximate $\theta \approx \pi/2$, which implies

$$h \approx L_2, \quad \dot{h} \approx L_1 \dot{\theta}, \quad \ddot{h} \approx L_1 \ddot{\theta}. \quad (18)$$

The moment of inertia I_O is

$$I_O = mL_1^2 + \frac{1}{3}M_1(L_1 + l_2)^2 + M_2l_2^2. \quad (19)$$

Substituting Eqns. (15) and (18) into Eqn. (14) yields the dynamics,

$$\ddot{h} = \frac{1}{I_O} \left[\frac{16h^2TL_1^2}{16h^2 - R^2} - l_1L_1g(m + M_1) + l_2L_1gM_2 \right] - b_1'\dot{h}, \quad (20)$$

where $b_1' = b_1/I_O$. Note that in the limit as the mass M_1 of the compound pendulum setup and the mass of the counterweight M_2 go to zero, i.e., if we ignore the mass of the support structure, the compound pendulum dynamics in Eqn. (20) reduce to the rotorcraft IGE dynamics given next.

Figure 5(a) shows the free-body diagram of a rotorcraft IGE. Applying Newton's second law in the \hat{e}_z direction yields

$$m\ddot{h} = T_{IGE} - mg - b_2\dot{h}, \quad (21)$$

where T_{IGE} is the rotor thrust IGE, m is the rotorcraft mass, \dot{h} and \ddot{h} are the vertical velocity and acceleration respectively, and b_2 is the damping coefficient due to aerodynamics. It is assumed henceforth that the rotorcraft has landed when $h/R = 0.5$, based on typical rotor distances above the landing gear. Thrust

IGE in Eqn. (15) is substituted into Eqn. (21) to obtain the dynamics of a rotorcraft IGE,

$$\ddot{h} = \frac{16h^2T}{(16h^2 - R^2)m} - g - b_2\dot{h}. \quad (22)$$

For the rotorcraft operating IGE, we define the state vector $Z \in \mathbb{R}^2$ and control input ν_1 as

$$Z = \begin{bmatrix} z_1 \\ z_2 \end{bmatrix} = \begin{bmatrix} h \\ \dot{h} \end{bmatrix} \quad \text{and} \quad \nu_1 = \frac{T}{m}. \quad (23)$$

The nonlinear state-space form of Eqn. (22) is

$$\dot{Z} = \begin{bmatrix} \dot{h} \\ \ddot{h} \end{bmatrix} = \begin{bmatrix} z_2 \\ \frac{16z_1^2}{16z_1^2 - R^2}\nu_1 - g \end{bmatrix}. \quad (24)$$

An equilibrium control input ν_1^* is necessary to keep the rotorcraft hovering at a corresponding equilibrium height z_1^* . Solving Eqn. (24) for the equilibrium condition, $\dot{Z}^* = 0$, the equilibrium control input is

$$\nu_1^* = g \frac{16z_1^{*2} - R^2}{16z_1^{*2}}. \quad (25)$$

Figure 5(b) depicts the simulation results of the open-loop nonlinear dynamics for an initial height and velocity of 1.5m and 0.25m/s, respectively, constant input $\nu_1 = \nu_1^*$ and $b_2 = 0$. In order to implement a linear controller for the nonlinear dynamics in Eqn. (24), the Jacobian matrices are needed. The Jacobians of Eqn. (24) evaluated at the equilibrium condition are

$$A = \begin{bmatrix} 0 & 1 \\ \frac{-2gR^2}{z_1^*(16z_1^{*2} - R^2)} & 0 \end{bmatrix} \quad \text{and} \quad B = \begin{bmatrix} 0 \\ \frac{16z_1^{*2}}{16z_1^{*2} - R^2} \end{bmatrix}. \quad (26)$$

The eigenvalues of A are pure imaginary, corresponding to a center, which implies the system oscillates around the equilibrium height.

Height and Velocity Estimation using a Bayesian Filter

The Bayesian filter [19, 25] is a probabilistic approach for estimation that assimilates noisy measurements into a probability density function (PDF) using nonlinear system dynamics and observation operators. The optimal Bayesian filter for linear systems with linear measurements and Gaussian noise is the Kalman filter [26], whereas a common Bayesian filter for nonlinear systems with nonlinear observation and noise models is the particle filter [27]. For the purpose of height estimation, a grid-based recursive Bayesian filter is rapidly implemented for a low-dimensional state-space representation of the rotorcraft downwash, ensuring temporal integration of the estimated height as it evolves over time.

The Bayesian framework consists of an estimation step and a prediction step. In the estimation step, the Bayesian filter [19] estimates the vehicle height based on the flow measurements collected from an array of differential pressure sensors. The finite parameter space over height h is discretized and the probability density is evaluated on this grid for each new measurement. The flow measurement \tilde{V} is assumed to be corrupted with zero mean Gaussian noise as in Eqn. (12). Let $L = \{\tilde{V}_1, \dots, \tilde{V}_m\}$ denote the set of measurements from m sensors. The posterior probability density of the state h given the measurements L is [19]

$$p(h|L) = cp(L|h)p(h|L_0), \quad (27)$$

where c is the scaling factor chosen so that the posterior $p(h|L)$ has unit integral over the state space. The likelihood function $p(L|h)$ is the conditional probability of the observations L given the state h and $p(h|L_0)$ represents the prior probability density, initially a uniform distribution.

We choose a Gaussian likelihood function for the measurements $\tilde{V}_l, l = 1, \dots, m$, i.e.,

$$p(\tilde{V}_l|h) = \frac{1}{\sqrt{2\pi}\sigma_m} \exp \left[-\frac{1}{2\sigma_m^2} (\tilde{V}_l - V_l)^2 \right], \quad (28)$$

where V_l is the flow at height h generated from Eqns. (10) or (11) at the location of sensor l and σ_m^2 is the expected measurement variance. The posterior probability density of the state h is obtained using the

joint measurement likelihood combining the measurements taken from all m sensors [19], i.e.,

$$p(h|L) = c \left(\prod_{l=1}^m p(\tilde{V}_l|h) \right) p(h|L_0). \quad (29)$$

The estimated height \hat{h} corresponding to the mode of the posterior probability $p(h|L)$ provides the maximum likelihood estimate of the flowfield parameters. Spatial integration over the sensor array is accomplished by Eqn. (29), whereas temporal integration is accomplished by assigning the posterior of the current time step to be the prior for the next time step.

The Bayesian prediction step consists of shifting and diffusing the probability mass to account for the vehicle dynamics using the Chapman-Kolmogorov equation [27],

$$\begin{aligned} p(h(t + \Delta t)|L(t)) \\ = \int p(h(t + \Delta t)|h(t))p(h(t)|L(t))dh(t), \end{aligned} \quad (30)$$

where t is the time step and Δt is the time step interval. In our case, the probability density is shifted along the grid according to the estimated vertical velocity \hat{z}_2 . The number of grid points to shift is determined by the product of the estimated velocity \hat{z}_2 and time interval. After shifting, the probability density is normalized to ensure the PDF integrates to one. To account for uncertainty in the motion model, the probability density is diffused by convolution with a grid-sized Gaussian to simulate process noise.[†] The window width is inversely proportional to the process noise standard deviation σ_p .

The vertical velocity \hat{z}_2 is estimated from the estimated height \hat{z}_1 by finite differencing, i.e.,

$$\hat{z}_{2,p} = \alpha \hat{z}_{2,p-1} + (1 - \alpha) \frac{\hat{z}_{1,p} - \hat{z}_{1,p-1}}{\Delta t}, \quad (31)$$

where $0 < \alpha < 1$ and the index p indicates the current iteration. Equation (31) is a low-pass-filter that removes most of the effects of high-frequency noise.

The measurement and process noise in the Bayesian filter are used as tuning knobs to improve the filter performance in terms of estimation accuracy and convergence speed. Statistical analysis of the measurements in hover was used to determine the nominal values. For example, decreasing or increasing

[†]This step is done with the MATLAB functions `gausswin` and `convn`.

the measurement noise variance σ_m^2 relative to the process noise variance σ_p^2 speeds up or slows down, respectively, the filter's response to measurements.

In order to design a fast observer that does not react to outlier measurements, the measurements are pre-filtered before they are passed into the Bayesian filter. Given the corrupted measurement \tilde{V} from Eqn. (12), the goal is to compute an estimate \hat{V} of the original velocity component signal V through signal reconstruction, which is also known as de-noising or smoothing [28]. The quadratic smoothing convex optimization method is implemented using the quadratic smoothing function [28]

$$\Lambda(V) = \sum_{p=1}^{n-1} (V_{p+1} - V_p)^2 = \|DV\|_2^2, \quad (32)$$

where V is the velocity component signal we wish to reconstruct and $D \in \mathbb{R}^{(n-1) \times n}$ is the bidiagonal matrix

$$D = \begin{bmatrix} -1 & 1 & 0 & \dots & 0 & 0 & 0 \\ 0 & -1 & 1 & \dots & 0 & 0 & 0 \\ \dots & \dots & \dots & \dots & \dots & \dots & \dots \\ 0 & 0 & 0 & \dots & -1 & 1 & 0 \\ 0 & 0 & 0 & \dots & 0 & -1 & 1 \end{bmatrix}. \quad (33)$$

The optimal trade-off between $\|\hat{V} - \tilde{V}\|_2$ and $\|D\hat{V}\|_2$ is obtained by minimizing [28]

$$\|\hat{V} - \tilde{V}\|_2^2 + \delta \|D\hat{V}\|_2^2, \quad (34)$$

where $\delta > 0$ parametrizes the optimal trade-off curve. The solution to this quadratic problem is [28]

$$\hat{V} = (I + \delta D^T D)^{-1} \tilde{V}, \quad (35)$$

which can be efficiently computed, because $I + \delta D^T D$ is tridiagonal.

Figure 6 shows the comparison between measurements \tilde{V} and quadratically smoothed values of the velocity components \hat{V} , with $\delta = 500$. The trends of the measurements are still preserved in the smoothed values and the mean of both values are identical. Most importantly, the standard deviations of the smoothed values for v , w , and v_i are reduced compared to that of the measurements, which im-

proves the performance of the Bayesian filter.

Feedback Control Design

The controller is designed and implemented for height tracking operations, including hover, climb, descent, and landing. A Linear Quadratic Regulator (LQR) is verified in simulation, and a Proportional-Integral (PI) controller with feed-forward is implemented experimentally.

The state-space system of a rotorcraft IGE from Eqn. (24) in control-affine form is

$$\dot{Z} = f_1(Z) + f_2(Z)\nu_1, \quad (36)$$

where

$$f_1(Z) = \begin{bmatrix} z_2 \\ -g \end{bmatrix} \quad \text{and} \quad f_2(Z) = \begin{bmatrix} 0 \\ \frac{16z_1^2}{16z_1^2 - R^2} \end{bmatrix}. \quad (37)$$

Figure 5(b) shows that the constant-input open-loop nonlinear system with $\nu_1 = \nu_1^*$ oscillates about the equilibrium point, which implies that feedback control is needed to asymptotically stabilize z_1 to the desired height. A linear controller to be used with the nonlinear system dynamics is

$$\nu_1 = \nu_1^* + \Delta\nu_1, \quad (38)$$

where $\Delta\nu_1 = -K(Z - Z^*)$ and $K = [K_1 \quad K_2]$. The closed-loop dynamics with the linear state feedback controller in Eqn. (38) are

$$\dot{Z} = \begin{bmatrix} z_2 \\ -g \end{bmatrix} + \begin{bmatrix} 0 \\ \frac{16z_1^2}{16z_1^2 - R^2} \end{bmatrix} (\nu_1^* + \Delta\nu_1), \quad (39)$$

i.e.,

$$\dot{Z} = \begin{bmatrix} z_2 \\ -g + \frac{16z_1^2}{16z_1^2 - R^2} \left(g \frac{16z_1^{*2} - R^2}{16z_1^{*2}} - K_1(z_1 - z_1^*) - K_2 z_2 \right) \end{bmatrix}. \quad (40)$$

The gains K_1 and K_2 are chosen by LQR, using the A and B matrices in Eqn. (26). Figure 7 compares

the simulated nonlinear closed-loop dynamics in Eqn. (40) to the linear closed-loop dynamics using LQR with state feedback. Initial conditions for the height and velocity are (1.8m, 0.9m/s) and desired steady-state conditions are (0.75m, 0m/s). The closed-loop nonlinear (dashed) height h and vertical velocity \dot{h} converge to the desired steady state at 5s. The closed-loop linear dynamics (solid) display similar characteristics with the vertical velocity \dot{h} displaying more overshoot.

Figure 8 shows a simulation of the posterior probability density of estimated height during closed-loop ascent (Fig. 8(a)) and descent (Fig. 8(b)) using the Bayesian filter estimated height. Figure 8(a) shows an ascent maneuver from initial normalized height and velocity (with respect to R) of (0.7, 0/s) to a commanded height of 1.8m using process and measurement noise standard deviations of (0.1, 0.15/s). Figure 8(b) shows a descent maneuver from initial height and velocity of (1.8, 0.2/s) to a commanded height of 0.6 with process and measurement noise standard deviations of (0.08, 0.1/s). Figures 8(c,d) show the estimated speeds using the low-pass-filtered finite-differencing method in Eqn. (31) for ascent in (a) and descent in (b), respectively.

Figures. 8(a) and (b) show that the initial height estimation error is large, because the prior PDF is uniformly distributed. As the Bayesian filter assimilates measurements over time, the posterior probability density peaks and the estimated height converges to the actual height. As more measurements are taken, the filter narrows the probability density. Note that Fig. 8(a) has a bigger spread throughout its probability density distribution than Fig. 8(b), due to the higher noise variances.

Figures 8(c) and (d) show that the initial velocity estimates are relatively large as the difference between successive height estimations is also relatively large. This effect is influenced by the Bayesian filter initialization and also the controller, which is driving the system to the commanded height. As the system reaches steady state at about 4s, the velocity estimate begins to more closely track the actual velocity. The estimation may be improved by using a higher-fidelity flow model or additional flow sensors.

Experimental Methods and Results

Experiments were conducted to verify and implement the theoretical framework using a heave test stand for a rotorcraft IGE (without fuselage interference) as shown in Fig. 4(a). Figure 9(a) shows a block

diagram of the experimental instrumentation, which is categorized into three parts: sensing, estimation and control, and actuation. The differential-pressure probe sets (with Honeywell HSCDRRN001NDAA3 sensors) measure radial and vertical flow pressure. The differential-pressure measurements are collected by a microcontroller (Cortex-M4 Teensy 3.1) dedicated for data acquisition (DAQ), pre-filtering and conversion into velocity components via scaling by a calibration constant [17]. These velocity measurements are transmitted to the computer for height estimation and closed-loop control. The experimental setup is fabricated with MakerBeam and 80/20 modular aluminum profiles. The actuation of the experimental setup consists of a brushless DC motor (AC2830-358 850kV) and electronic speed controller (eRC Rapid Drive 25A) pair, which are powered by a DC power supply (Mastech HY3030E). Speed-control input requires Pulse Width Modulation (PWM) square wave signals with variable time scales, which are generated by the Remote Control (RC) receiver (Spektrum DX6i) or by a microcontroller (ATMega328 Arduino Nano) according to control inputs from the computer. All physical data connections are made through Universal Serial Bus (USB) cables. Note that the RC radio is used for manual motor-speed control, whereas the Arduino Nano microcontroller is used for automatic speed control. The carbon fiber rotor (HobbyKing 14 × 4.7) has a radius of $R = 0.1778\text{m}$ (7 in.).

A differential pressure probe set that is capable of measuring the radial and vertical differential pressure consists of two pairs of tubes, as shown in the magnified view of Fig. 9(b). Each pair is connected to a differential pressure sensor [17]. The pressure sensors are connected via an analog interface to the DAQ microcontroller. Since the pressure measurements are relatively noisy and the pressure sensors and DAQ microcontroller are capable of higher data rates than the estimation and control loop in the computer, a moving-average filter (MAF) is implemented on the pressure measurements to generate velocity measurements \tilde{V} . The MAF implementation is

$$\tilde{V} = \frac{a}{J} \sum_{j=1}^J \tilde{P}_j, \quad (41)$$

where \tilde{P}_j is the differential pressure sensor measurement j , J is the number of data points to average over, and a is the calibration constant to convert from differential pressure to velocity [17].

Figure 9(b) shows the instrumentation setup for the heave test stand. Precise real-time position (height

above the ground plane) of the rotor mount is obtained through the use of a motion-capture system (Opti-Track), which identifies and tracks reflective motion-capture markers attached to the probe bracket. Two different flow probe configurations are mounted on the probe bracket: the single pair and two-pair sets. A single probe pair is placed close to the rotor plane to measure the vertical differential pressure which corresponds to the induced velocity. This measurement is used as an input to the ring-source potential flow model in Eqns. (10) and (11). A two-pair probe set is used to measure the radial and vertical differential pressures. In order to reduce inter-probe interference, the induced velocity probe is mounted azimuthally 180° across from the two pair probe set; all probes are mounted above the probe bracket directly in the rotor flowfield.

Figure 10 compares the measured radial and vertical velocity components with the flow model at multiple radial stations for normalized height $h/R = 0.75$. The data is filtered with $J = 10^5$ data points in the moving-average filter in Eqn. (41). The average of five consecutive measurements are plotted. Error bars on the measured values show the values one standard deviation away from the mean. The probes are placed at vertical location $z/R = 0.18$ from the rotor plane, the motor rotational speed is $\omega = 2538$ RPM, and induced velocity IGE is $v_i = 4.34$ m/s. The induced velocity IGE is the average of vertical velocities close to the rotor plane across multiple radial locations and, in this case, the induced velocity probes are at vertical location $z/R = 0.05$.

The measured radial velocity v crosses over from positive to negative at $r/R = 0.75$, which represents suction toward the rotor hub. Taking the standard deviations into account, some of the radial measurements agree with the model, but the model does not predict the velocity sign changes. Due to the geometry of the ring sources, inward flows from opposite sides of the same ring cancel out and the radial velocity is always outward and positive. Furthermore, the radial flow is also influenced by turbulence and the tip vortices of each rotor blade, whereas the flow model only captures the mean velocity.

The measured vertical velocity w increases with increasing radial station from $r/R = 0.4$ to 0.75 and then decreases rapidly for the outboard section. The model predicts a similar trend of increasing vertical velocity with increasing radial station and gradually tapering off at approximately the same radial station as the measurement, but it still underpredicts the vertical velocity component. The underprediction is likely because the induced velocity used in this flow model is an average rather than the local value.

Model predictions are improved by using the local induced velocity as the input, as we show in the next experiment in this section. Some general trends of the steady flowfield are captured by this model, however some significant differences may persist due to the use of an average induced velocity and unmodeled effects, such as tip vortices. Despite these differences, use of the reduced-order model in the proposed estimation and control framework is sufficient for closed-loop heave control, presented later in this section.

Placing the probes within the rotor slipstream boundary, as shown in Fig. 11(a), improves the model-measurement match. Figure 12 compares the ring-source potential flow model (green) from Eqns. (10) and (11) with experimental results (blue) of radial v , vertical w , and induced v_i (red) velocity components for varying heights. Experiments were conducted on the heave test stand with probe vertical locations of $z/R = 0.10$ (solid circle), 0.20 (dashed diamond), $z_{v_i} = 0.08$, and radially symmetrical probe locations at (a)–(b) $(x, y) = (0, 0.47R)$, (c)–(d) $(x, y) = (0, 0.78R)$, and (e)–(f) $(x, y) = (0, 0.87R)$.

For probe locations at $(x, y) = (0, 0.47R)$, Fig. 12(a) shows relatively constant radial velocity v measurements for increasing height. The vertical velocity w measurements in Fig. 12(b) increase for increasing height and decreasing vertical probe location. The flow model captures the general trends, even though it overpredicts the radial velocity v and underpredicts the vertical velocity w , likely caused by the local induced velocity v_i at a radially symmetrical location being input into the flow model as opposed to the average for the previous experiment.

For probe locations at $(x, y) = (0, 0.78R)$, Fig. 12(c) shows that the radial velocity measurements v begin to fluctuate for decreasing vertical probe location, whereas the model stays relatively flat. The vertical velocity w measurements in Fig. 12(d) also display similar trends to that of (b) but they begin to decrease after $h/r = 1.5$, which is not captured by the model. The decrease in w and fluctuations in v are likely caused by the probes being closer to the edge of the slipstream boundary and being influenced by the effects of tip vortices. The slipstream boundary contracts more at greater heights and the ground effect becomes weaker, which causes the vertical velocity w to decrease as the probes are closer to the tip and the radial velocity v to fluctuate. Since the model does not include tip vortices, these detailed effects are not captured. The general trends are partially captured at this radial station for (c)–(d), albeit not as well as for the inboard case in (a)–(b).

Finally, for probe locations at $(x, y) = (0, 0.87R)$, Fig. 12(e) shows that the radial velocity v measure-

ments decrease with increasing height for $z/R = 0.20$ and increase slightly with decreasing height for $z/R = 0.10$. The general trend is similar for the model, which still overpredicts the measurements. The vertical velocity w measurements in Fig. 12(f) for both vertical sensor locations decrease with increasing heights. However, the model diverges from the measurement trends and its vertical velocity w increases with increasing height and then tapers off. The divergence is likely caused by the (outboard) probe being outside the slipstream boundary, as shown in Fig. 11(a). Once the probe is outside the slipstream boundary, it no longer measures the flowfield due to ground effect, but rather the flowfield outside the rotor wake, which is not modeled.

Probe placement has a significant effect on model-measurement mismatch. In fact, a nominal 12% increase in the radial location from $y = 0.78R$ to $0.87R$ causes the probe to exit the slipstream boundary. Hence, as shown in Fig. 11(b), the probes were placed in a radially symmetrical fashion at about mid-radius where tip effects are not significant and the model captures the general trends of the measurements within the operational region of ground effect.

The following experiment was conducted for the purpose of validating the height-estimation framework. The experiment tested the flow-sensing based Bayesian height estimation separately from the closed-loop control by using the actual height provided by motion capture. The grid-based recursive Bayesian height estimation was implemented with Eqn. (29) and the closed-loop control was performed with a PI-feed-forward controller described below, using height feedback from the motion-capture system. The probes are radially symmetrical at $(x, y) = (0, 0.47R)$, $z/R = 0.2$ and $z_{vi}/R = 0.08$. The standard deviation for measurement (v, w) and process noise are (4.8, 2.4, 10). The measurements are pre-filtered by means of $J = 50$ points in the MAF of Eqn. (41) and $\delta = 500$ for quadratic smoothing (35).

Figure 13 shows the experimental results for the height-estimation framework. Figure 13(a) shows the commanded heights in black. The heave stand was initiated at normalized height $z/r = 0.75$, increased to $z/r = 1.6$, then decreased to $z/R = 1$. The height estimates (blue) are plotted against ground truth (red). The filter response converges to the true height and is capable of tracking commanded height changes. Figure 13(b) shows the percentage estimation error between the estimated and actual height, with zero mean error in this sample run. The mean estimation errors observed over multiple runs were less than 5% (1.1cm or 0.44in). Most estimation errors were within the $\pm 20\%$ range. As the system settled towards a

steady-state height or the system velocity is sufficiently slow, the estimation converged, as can be seen at 30s and 65s.

Figure 13(c) shows the measured (dash-dot) and model (solid) radial v velocity. Figure 13(d) shows the measured (dash-dot) and model (solid) vertical w velocity as well as the induced velocity v_i (dash). The model velocity components plotted are the components corresponding to the estimated height with the induced velocity as input. Note that the estimation error is smallest when the flow model closely matches the measured velocities, which improves the ability of the Bayesian filter to localize the true system state.

Figure 13(e) shows the posterior PDF of the Bayesian height estimator. For $t \leq 20$ s, the heave stand does not move from $z/R = 0.7$; the filter is confident in its estimate, as shown by the color map. As the heave stand ascends, the filter converges quickly because the PDF has less spread. From $t = 20$ s to 60s, the heave stand makes small corrections that are tracked by the filter. Similar performance is observed for the descent maneuver, where the filter estimate converges to the actual height between $t = 65$ s to 85s.

The final experiment was conducted to validate the entire observer-based height-tracking framework using Bayesian height estimation and feedback-feed-forward control. This experiment is similar to the experiment conducted in the previous subsection, but the height for feedback control was provided by the Bayesian filter in this case. All other parameters are the same.

A Proportional Integral (PI) controller with feed-forward control was implemented on the heave test stand. The heave test stand is actuated with a brushless DC motor that is controlled with an electronic speed controller, which takes PWM signals as control input for motor rotational speed regulation. The PWM control input from feedback control is computed as

$$\nu_{PI} = K_P(z_1^* - \hat{z}_1) + K_I \int (z_1^* - \hat{z}_1) dt, \quad (42)$$

where K_P and K_I are the proportional and integral gains. A block diagram of the closed-loop control system is shown in Fig. 14.

Feed-forward control is typically used to speed up the closed-loop system response and compensate for unmodeled dynamics by feeding in set inputs. We implemented the feed-forward controller in order to compensate for the transient dynamics of the motor/speed-controller pair, which is not modeled. The feed-forward control input ν_{FW} was based on a curve fit for the open-loop transient PWM-height curve.

The sum of the feedback and feed-forward control inputs

$$\nu_2 = \nu_{PI} + \nu_{FW} \quad (43)$$

is rate limited and saturated before being sent to the speed controller. The rate limiter and the saturation block are implemented to ensure that the test stand stays within the operational region of ground effect.

Figure 15 shows the experimental results, which validate the feedback and feed-forward control framework. Figures 15(a)–(d) show the same plots as Figs. 13(a)–(d), with the exception that this maneuver is for observer-based closed-loop control. Figure 15(e) shows the PWM commands for various terms, including control input ν_2 (blue), feed-forward term (magenta) and desired control input (blue) before being rate limited and saturated between 110-126 PWM (dashed black). Loop speed of 39 loops/s is achieved. Figure 15(f) shows the percentage motion error between desired height and actual height.

The mean estimation and motion errors for this sample case are 4% and 7% respectively. As before, most of the estimation and motion errors fall within the $\pm 20\%$ range. The biggest estimation and motion errors result from changes in the commanded height around 18s and 55s. For multiple runs with the same parameters, the mean estimation errors are less than 5% (1.1 cm or 0.44in.) and the motion errors are less than 9% (2 cm or 0.79 in.). Another factor to consider beyond unsteady aerodynamics, tip effects and measurement and process noise when evaluating the cause of estimation errors is that the estimation error is close to the mean probe tip-to-tip length of 1.2 cm, which is in effect the average resolution of the probes.

Figure 15(g) shows the posterior of the Bayesian filter used for closed-loop control, with two step inputs at $t = 18\text{s}$ and 55s . In general, the filter tracks height changes well and converges to the actual height quickly. From $t = 25$ to 35s , the feedback controller drives the estimated height to the commanded height. The system settles into steady-state height at 40s , when the filter converges to the actual height and the closed-loop control is capable of driving the system to the desired height.

Conclusions

This paper describes a flow-sensing and control framework for rotorcraft height stabilization in ground effect and provides experimental demonstration for application to a MAV-scale autonomous rotorcraft. We show that height estimation and closed-loop control are feasible by measuring from two sets of differential pressure probes and comparing to a reduced-order aerodynamic model within a Bayesian filter framework with linear feedback control. Additional conclusions of this paper are as follows:

1) A ring-source potential flow model for the rotor downwash IGE captures basic characteristics of the relationship between flow velocity and height, and can be recursively evaluated in real-time at up to 39 loops per second. With model inputs of rotor induced velocity, probe radial and vertical locations, the flow model has been experimentally validated. The flow model best predicts the flowfield with induced velocity and radial-vertical velocity measurements collected mid-radius of the rotor.

2) A nonlinear dynamic model of the heave test stand, which reduces to the dynamics of a rotorcraft landing IGE, allows for the study of the open-loop dynamics and facilitates the design of a closed-loop controller. It is found that the constant-input open-loop height of a rotorcraft IGE oscillates about an equilibrium point, which corresponds to a center fixed point. Hence, a closed-loop controller is required for height tracking operations IGE.

3) The height of the rotorcraft IGE is experimentally estimated with a grid-based recursive Bayesian filter using the flow model and differential-pressure probe measurements. It is found that the measurements should be pre-filtered with a moving-average filter and a quadratic smoothing function in order to obtain higher fidelity estimates. The measurement and process noise variances can be used as tuning knobs to improve estimation accuracy and convergence speed.

4) A linear quadratic regulator for height tracking was verified in simulation. Experimentally, flow-estimation-based closed-loop control is implemented using a feedback and feed-forward design. The feedback and feed-forward combination was necessary to compensate for unmodeled motor dynamics with a short transient response.

5) The mean experimental estimation error is no greater than 5% (1.1 cm or 0.44 in.) and the mean

motion error is no greater than 9% (2 cm or 0.79 in.). Despite unsteady aerodynamics, tip effects, and measurement and process noise, the estimation error is close to the probe resolution, which is its tip-to-tip length of 1.2 cm. The experiments demonstrate that the flow sensing-based height estimation and control framework is viable, with applications in autonomous rotorcraft landing.

Acknowledgments

The authors gratefully thank William Craig, Derrick Yeo, Daigo Shishika, Feitian Zhang, and Nitin Sydney for valuable discussions and assistance. This work was supported by the University of Maryland Vertical Lift Rotorcraft Center of Excellence Army Grant No. W911W61120012.

References

- ¹Tritschler, J., "Contributions to the Characterization and Mitigation of Rotorcraft Brownout," Doctor of Philosophy Dissertation, Department of Aerospace Engineering, University of Maryland, 2012.
- ²Plank, V.G., Spatola, A.A., and Hicks, J.R., "Fog Modification by Use of Helicopters," Air Force Cambridge Research Laboratories, U.S. Army Atmospheric Sciences Laboratory, AFCRL-70-0593, Environmental Research Papers No. 335, ECOM-5339, Oct. 1970.
- ³Serra, P., Cunha, R., and Silvestre, C., "On the Design of Rotorcraft Landing Controllers," 16th Mediterranean Conference on Control and Automation, Ajaccio France, June 2008.
- ⁴Mahony, R., and Hamel, T., "Adaptive Compensation of Aerodynamic Effects during Takeoff and Landing Manoeuvres for a Scale Model Autonomous Helicopter," *European Journal of Control*, (2001) 0:1-15, 2001.
- ⁵Nonaka, K., and Sugizaki, H., "Integral Sliding Mode Altitude Control for a Small Model Helicopter with Ground Effect Compensation," American Control Conference, San Francisco CA, June 2011.
- ⁶Hu, B., Lu, L., and Mishra, S., "A Control Architecture for Fast and Precise Autonomous Landing of a VTOL UAV onto an Oscillating Platform," 71st American Helicopter Society Society Annual Forum, Virginia Beach VA, May 2015.

⁷Borenstein, J., and Koren, Y., "Obstacle Avoidance with Ultrasonic Sensors," *IEEE Journal for Robotics and Automation*, Vol. 4, No. 2, April 1988.

⁸Tanigawa, M., Luinge, H., Schipper, L., and Slycke, P., "Drift-Free Dynamic Height Sensor using MEMS IMU Aided by MEMS Pressure Sensor," Proceedings of the 5th Workshop on Positioning, Navigation and Communication, 2008.

⁹Lee, T.E., Leishman, J.G., and Ramasamy, M., "Fluid Dynamics of Interacting Blade Tip Vortices with a Ground Plane," *Journal of the American Helicopter Society* 55, 022005, 2010.

¹⁰Tanner, P.E., Overmeyer, A.D., Jenkins, L.N., Yao, C.S., and Bartram, S.M., "Experimental Investigation of Rotorcraft Outwash in Ground Effect," 71st American Helicopter Society Society Annual Forum, Virginia Beach VA, May 2015.

¹¹Prouty, R.W., *Helicopter Performance, Stability, and Control*, Krieger Publishing Company, Florida, 2002.

¹²Govindarajan, B., "Evaluation of Particle Clustering Algorithms in the Prediction of Brownout Dust Clouds," Master's Thesis, Department of Aerospace Engineering, University of Maryland, August 2011. Available online: <http://drum.lib.umd.edu/handle/1903/11846>

¹³Kalra, T. S., "CFD Modeling and Analysis of Rotor Wake in Hover Interacting with a Ground Plane," Doctor of Philosophy Dissertation, Department of Aerospace Engineering, University of Maryland, 2014. Available online: <http://drum.lib.umd.edu/handle/1903/16086>

¹⁴Cheeseman, I.C., and Bennett, W.E., "The Effect of the Ground on a Helicopter Rotor in Forward Flight," Reports & Memoranda No. 3021, Ministry of Supply, Aeronautical Research Council Reports and Memoranda, Sept. 1955.

¹⁵Knight, M., and Hefner, R. A., "Analysis of Ground Effect on the Lifting Airscrew," NACA TN 835, 1941.

¹⁶Rossow, V. J., "Effect of Ground and/or Ceiling Planes on Thrust of Rotors in Hover, NASA TM 86754, 1985.

¹⁷Yeo, D. W., Sydney, N., Paley, D., and Sofge, D., "Onboard Flow Sensing For Downwash Detection and Avoidance On Small Quadrotor Helicopters," Proc. AIAA Guidance, Navigation and Control Conf., number AIAA-2015-1769, pages 1-11, Orlando FL, Jan. 2015.

¹⁸Lagor, F.D., DeVries, L.D., Waychoff, K., and Paley, D.A., “Bio-inspired Flow Sensing and Control: Autonomous Rheotaxis Using Distributed Pressure Measurements,” *Journal of Unmanned System Technology*, 1(3):78–88, 2013.

¹⁹DeVries, L.D., Lagor, F.D., Lei, H., Tan, X., and Paley, D.A., “Distributed Flow Estimation and Closed-Loop Control of an Underwater Vehicle with a Multi-Modal Artificial Lateral Line,” *Bioinspiration & Biomimetics*, 10(2):1-15, 2015.

²⁰Hooi, C.G., Lagor, F., and Paley, D., “Flow Sensing, Estimation and Control for Rotorcraft in Ground Effect,” IEEE Aerospace Conference, Big Sky MT, March 2015.

²¹Hooi, C.G., “Design, Rapid Prototyping and Testing of a Ducted Fan Microscale Quadcopter,” 70th American Helicopter Society Society Annual Forum & Technology Display, Montreal QC, May 2014.

²²Hooi, C.G., Lagor, F., and Paley, D., “Flow Sensing, Estimation and Control for Rotorcraft in Ground Effect: Modeling and Experimental Results,” 71st American Helicopter Society Society Annual Forum, Virginia Beach VA, May 2015.

²³Leishman, J.G., *Principles of Helicopter Aerodynamics*, 2nd. Ed., p.258 - 260, Cambridge University Press, New York, 2006.

²⁴Hess, J.L., and Smith, A.M.O., “Calculation of Potential Flow about Arbitrary Bodies,” *Progress in Aerospace Sciences*, Volume 8, p. 39-40, 1967.

²⁵Murphy, K., *Machine Learning: A Probabilistic Perspective*, The MIT Press, Cambridge MA, 2012.

²⁶Simon, D., *Optimal State Estimation: Kalman, H Infinity, and Nonlinear Approaches*, 1st. Ed., p.465-466, John Wiley & Sons, Inc., New Jersey, 2006.

²⁷Arulampalam, M.S., Maskell, S., Gordon, N., and Clapp, T., “A Tutorial on Particle Filters for Online Nonlinear/Non-Gaussian Bayesian Tracking,” *IEEE Transactions on Signal Processing*, Vol. 50, No. 2, Feb. 2002.

²⁸Boyd, S., and Vandenberghe, L., *Convex Optimization*, p.312, Cambridge University Press, 2014.

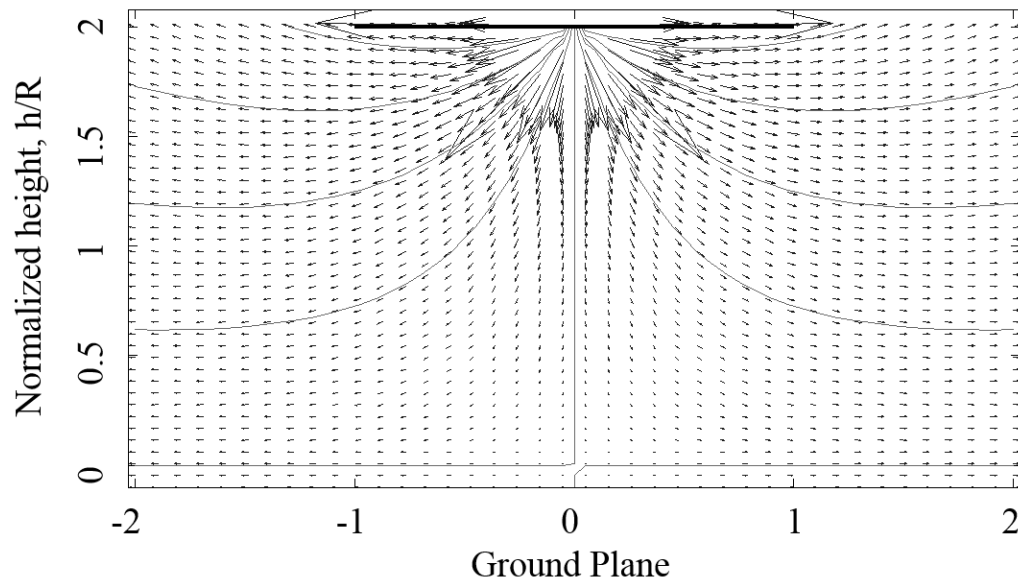


Fig. 1 Cheeseman and Bennett [14] potential flow model of rotor downwash in ground effect.

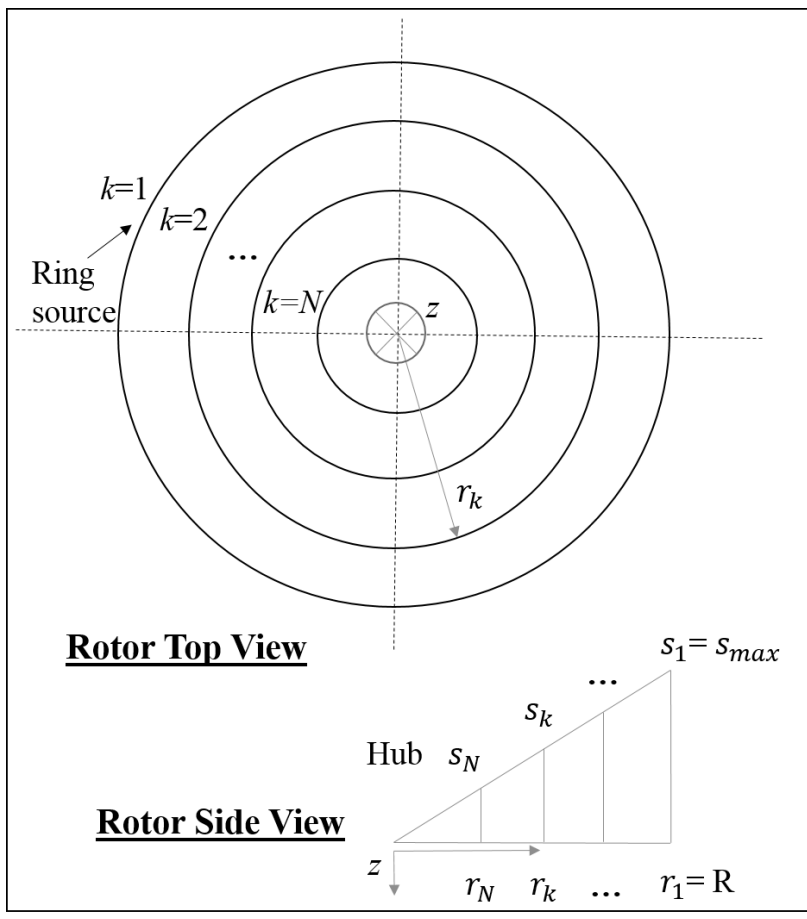


Fig. 2 Schematic of ring-source potential-flow nomenclature.

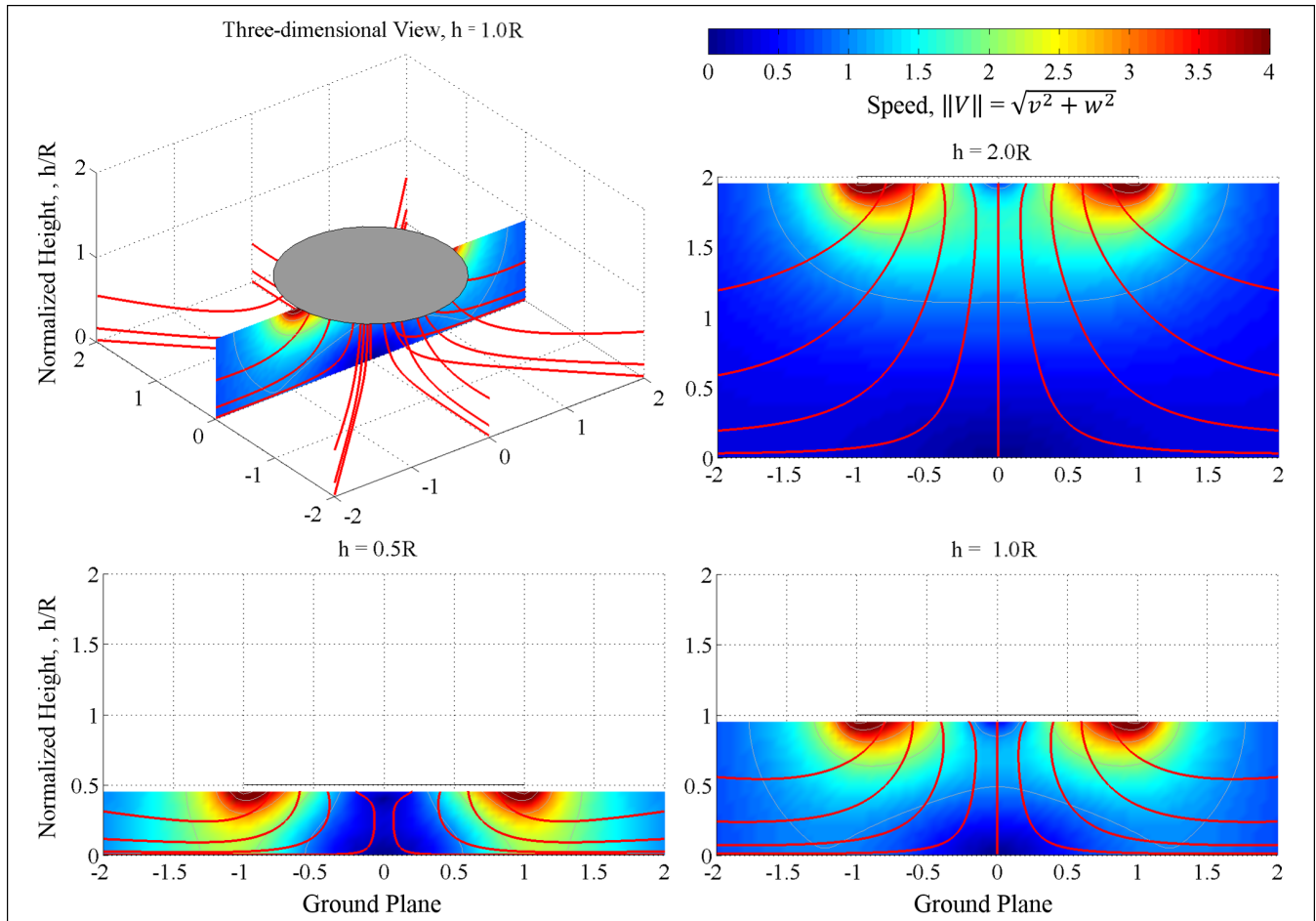


Fig. 3 Flowfield of ring-source potential flow evaluated at various heights, depicting streamlines and speed distributions; flow speed is $\|V\| = \sqrt{v^2 + w^2}$.

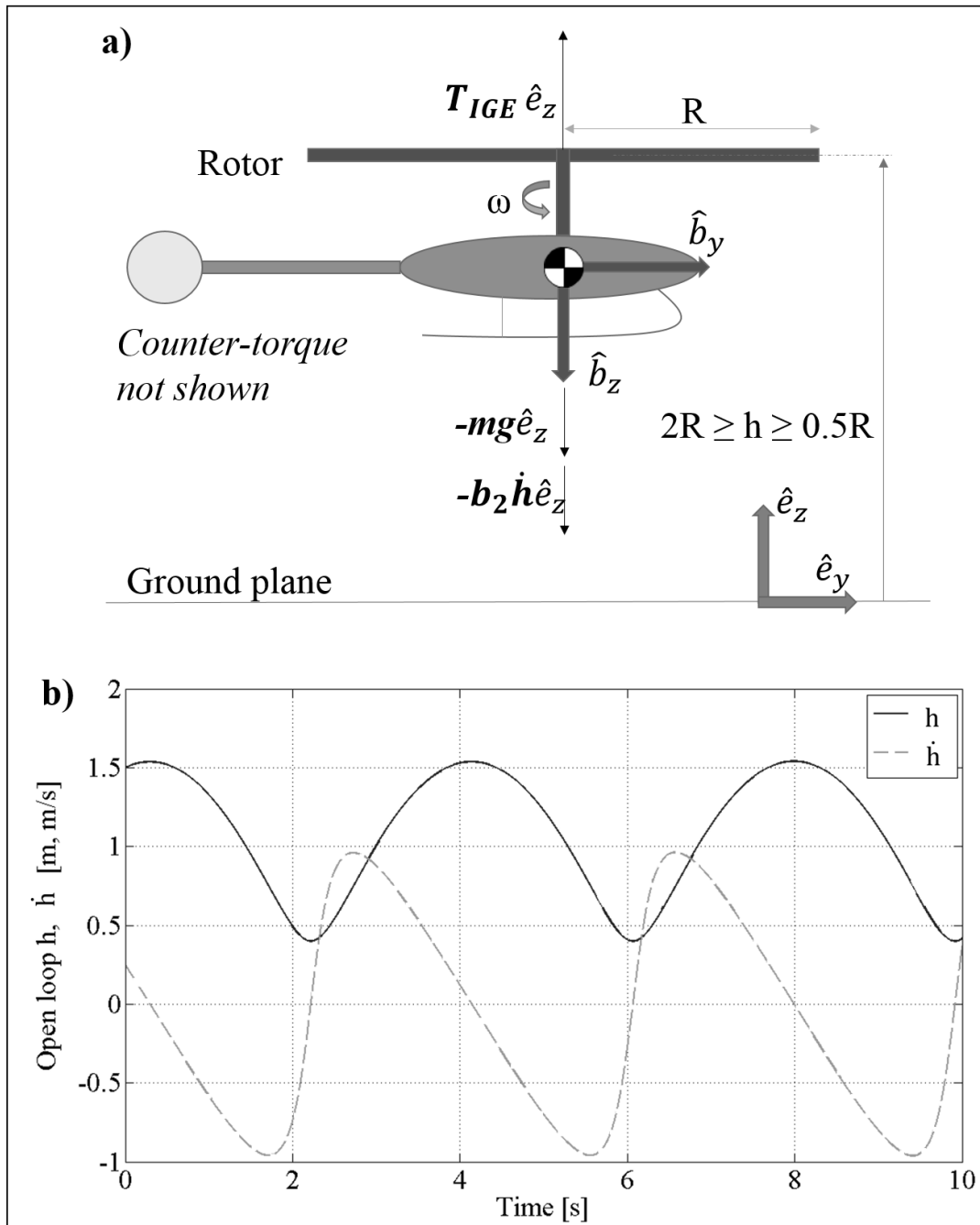


Fig. 5 (a) Free-body diagram of rotorcraft in ground effect. (b) Open-loop dynamics of rotorcraft in ground effect with constant input $\nu_1 = \nu_1^*$ and no damping. Initial conditions for height and velocity are 1.5m and 0.25m/s, respectively.

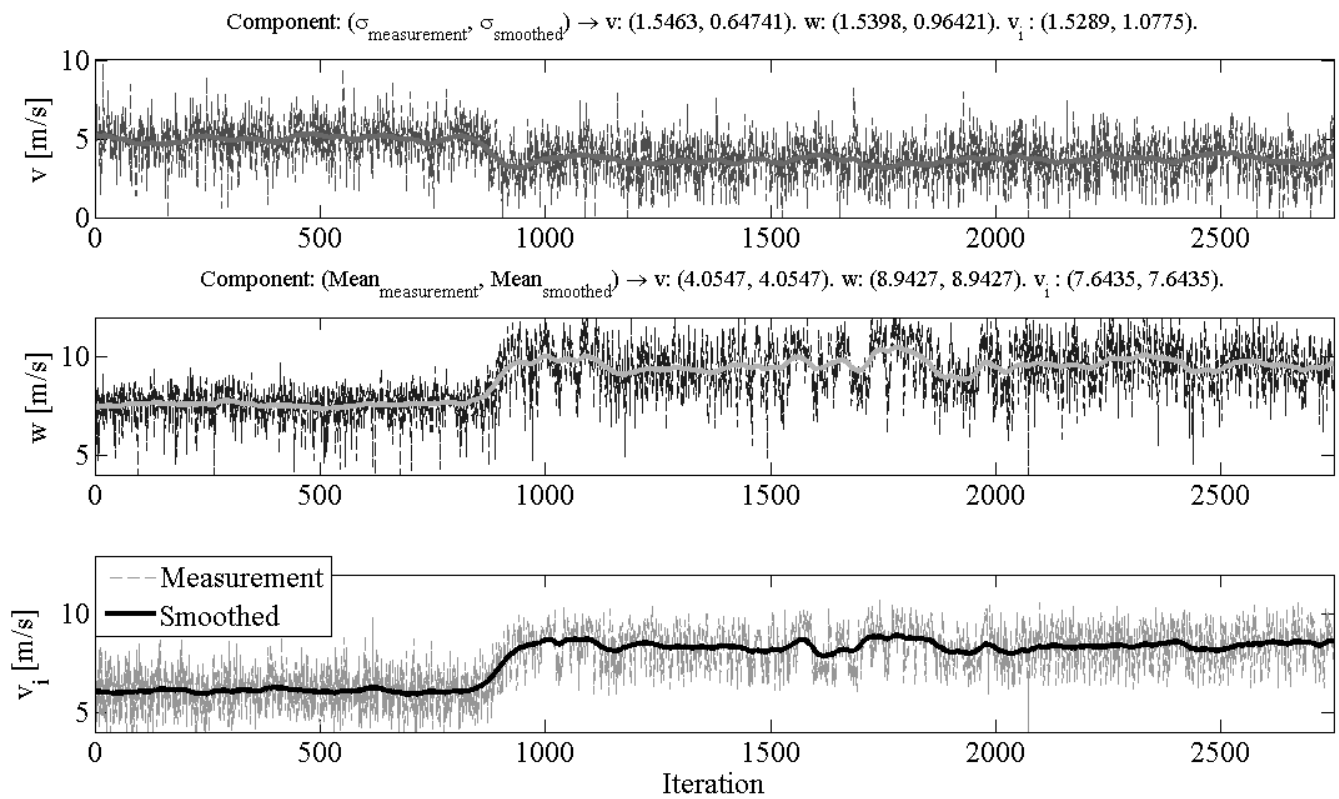


Fig. 6 Comparison between measurements and quadratically smoothed values of velocity components.

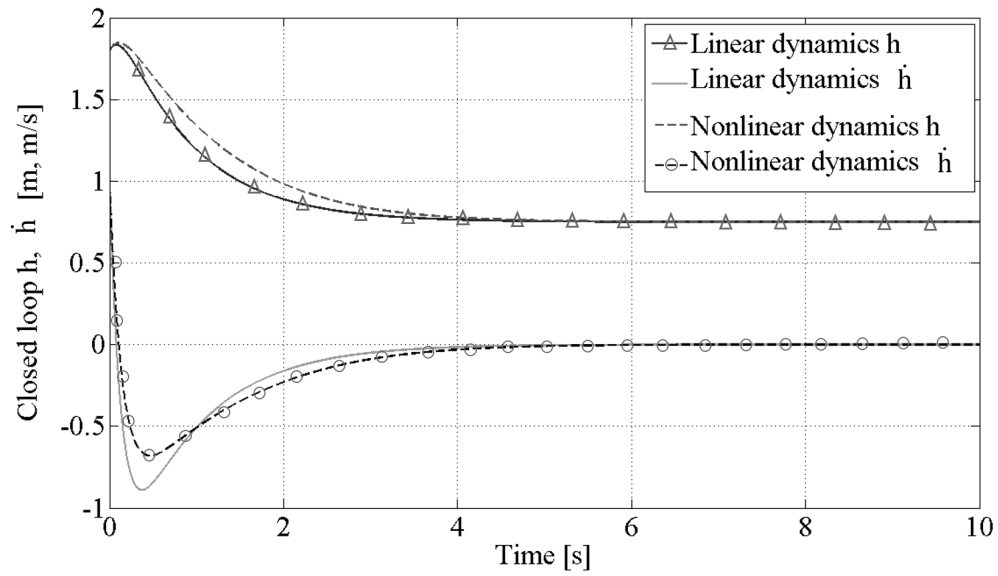


Fig. 7 Simulated closed-loop dynamics of rotorcraft in ground effect with no damping using the state feedback linear controller in Eqn. (38).

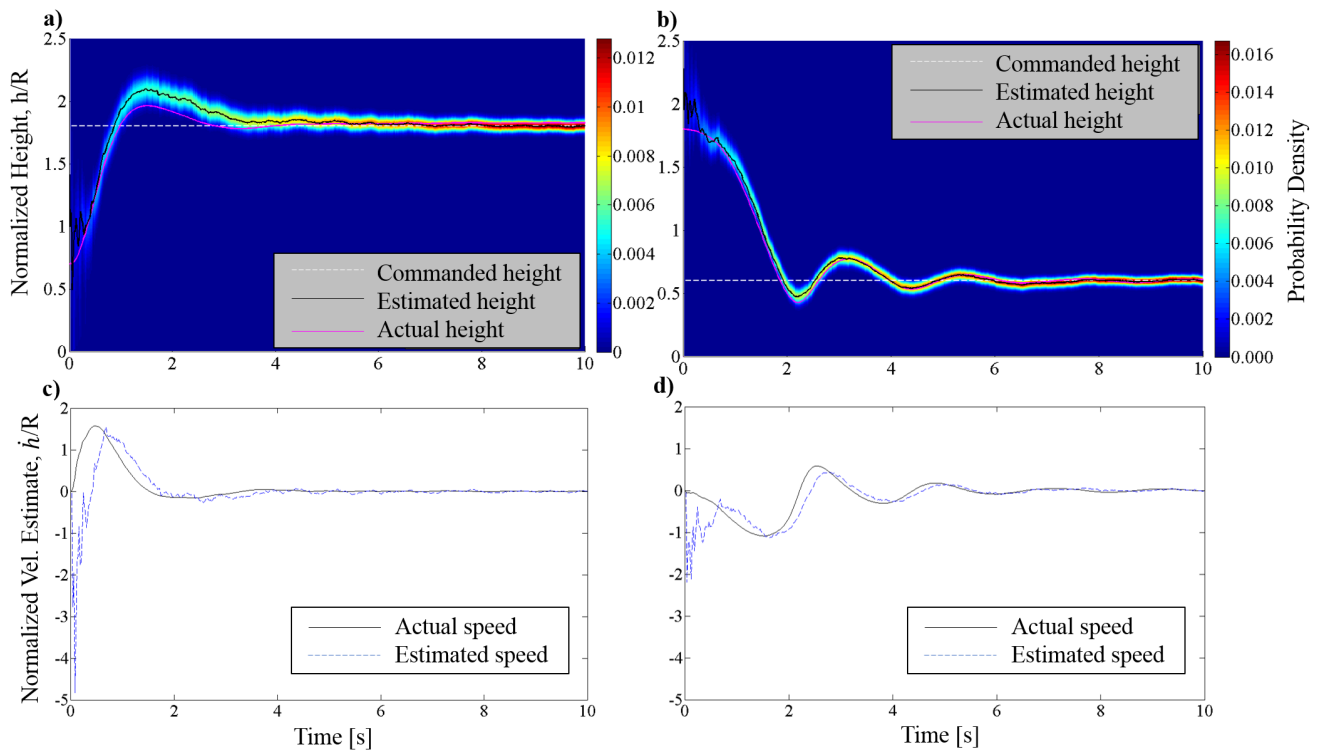


Fig. 8 Simulations of the closed-loop system using the estimated height from the Bayesian filter. History of posterior PDF of normalized height h/R for (a) ascent maneuver from initial height and velocity of $(0.7, 0/s)$, commanded height of 1.8, $(\sigma_p, \sigma_m) = (0.1, 0.15/s)$; (b) descent maneuver from initial height and velocity of $(1.8, 0.2/s)$, commanded height of 0.6, $(\sigma_p, \sigma_m) = (0.08, 0.1/s)$. Estimated velocities with low-pass-filtered finite differencing for (a) and (b) are shown in (c) and (d).

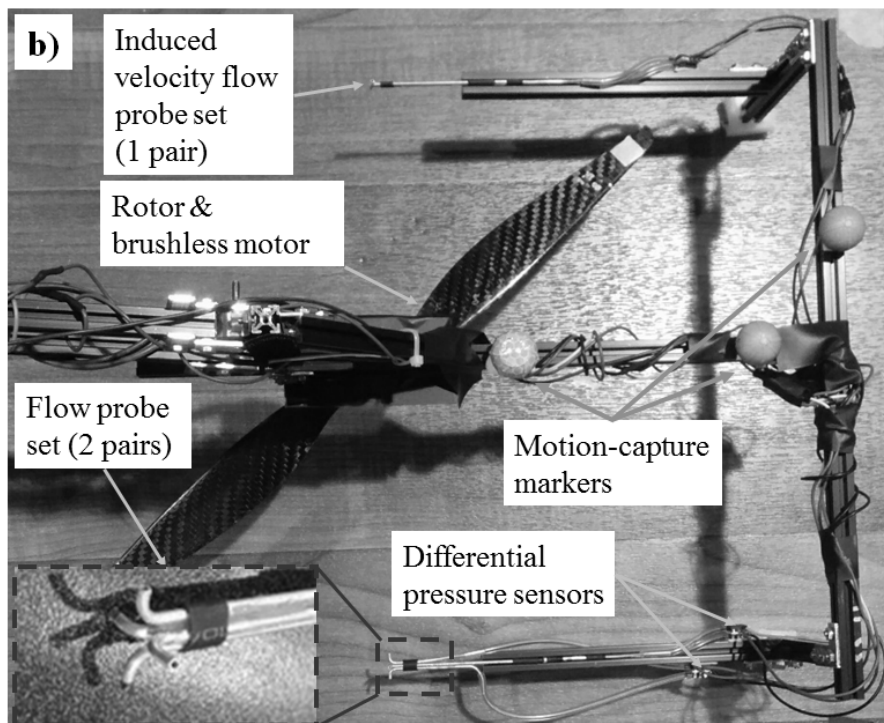
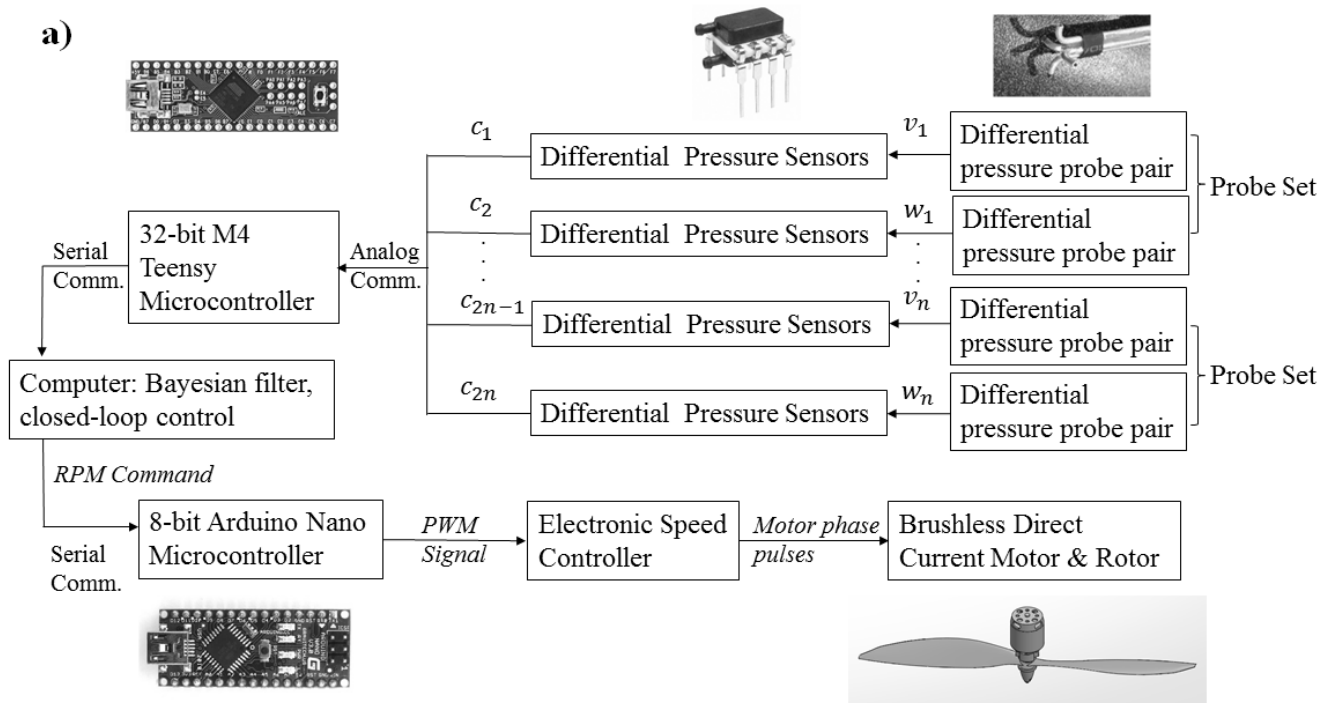


Fig. 9 (a) Block diagram for experimental instrumentation. (b) Heave test stand instrumentation with magnified view of two-pair differential pressure probe set providing radial and vertical velocity components.

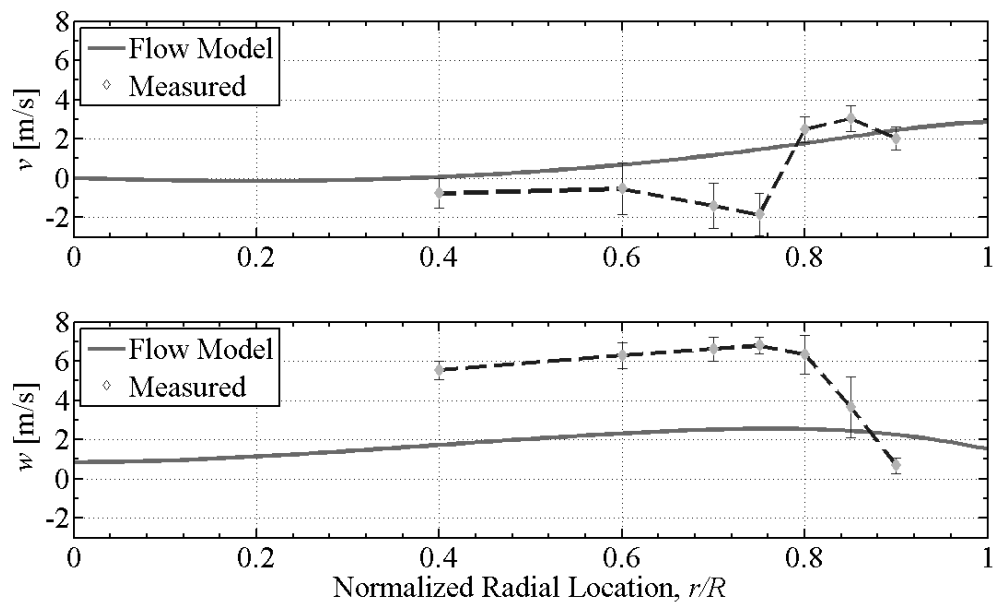


Fig. 10 Comparison between ring-source potential flow model in Eqns. (10), (11) and experimental results of radial v and vertical w velocity components for various radial locations. Error bars denote one standard deviation from the mean. Normalized height $h/R = 0.75$, normalized probe location $z/R = 0.18$, rotational speed $\omega = 2538$ RPM, induced velocity IGE $v_i = 4.34$ m/s.

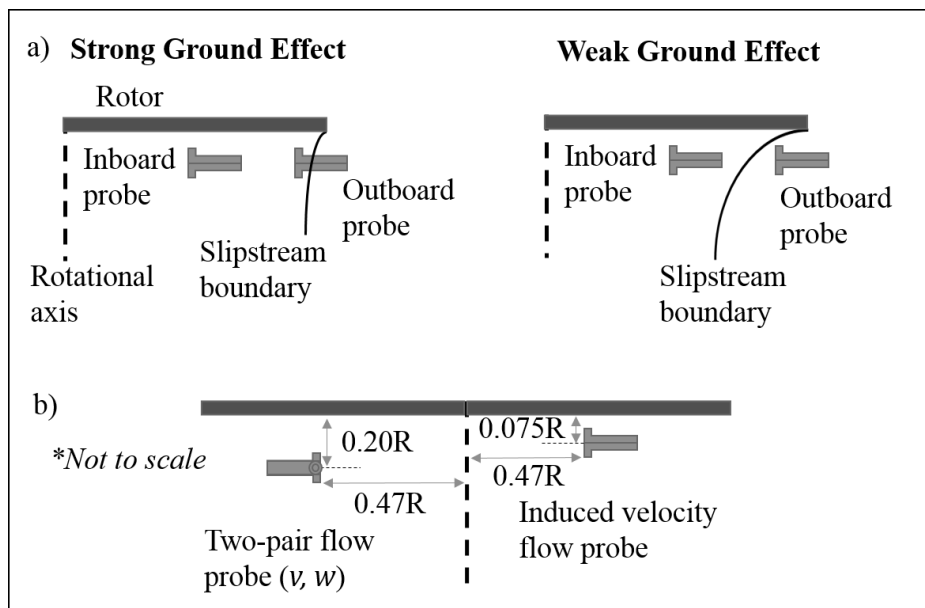


Fig. 11 (a) Probe placement in strong and weak ground effect. (b) Rotor side-view showing mid-radius location with radial symmetry for two-pair flow probes (radial v and vertical w velocity components) and induced velocity v_i flow probe.

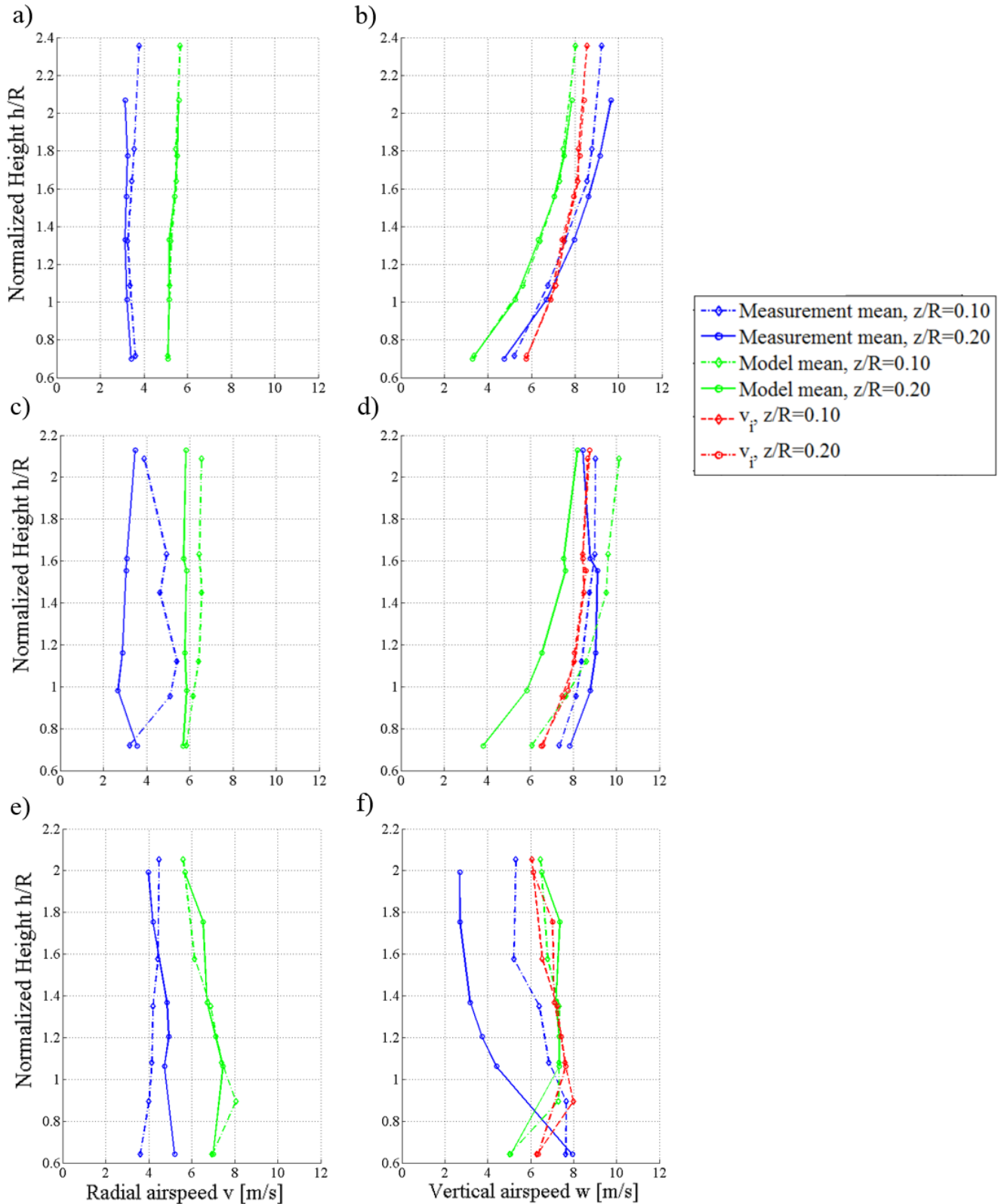


Fig. 12 Comparison between ring-source potential flow models (green) and experimental results (blue) of radial v , vertical w and induced v_i (red) velocity components for varying heights. Experiments were conducted on the heave test stand with probe vertical locations of $z/R = 0.10$ (solid circle), 0.20 (dashed diamond) and $z_{v_i} = 0.08$. The probes are radially symmetrical at (a)–(b) $(x, y) = (0, 0.47R)$; (c)–(d) $(x, y) = (0, 0.78R)$; (e)–(f) $(x, y) = (0, 0.87R)$.

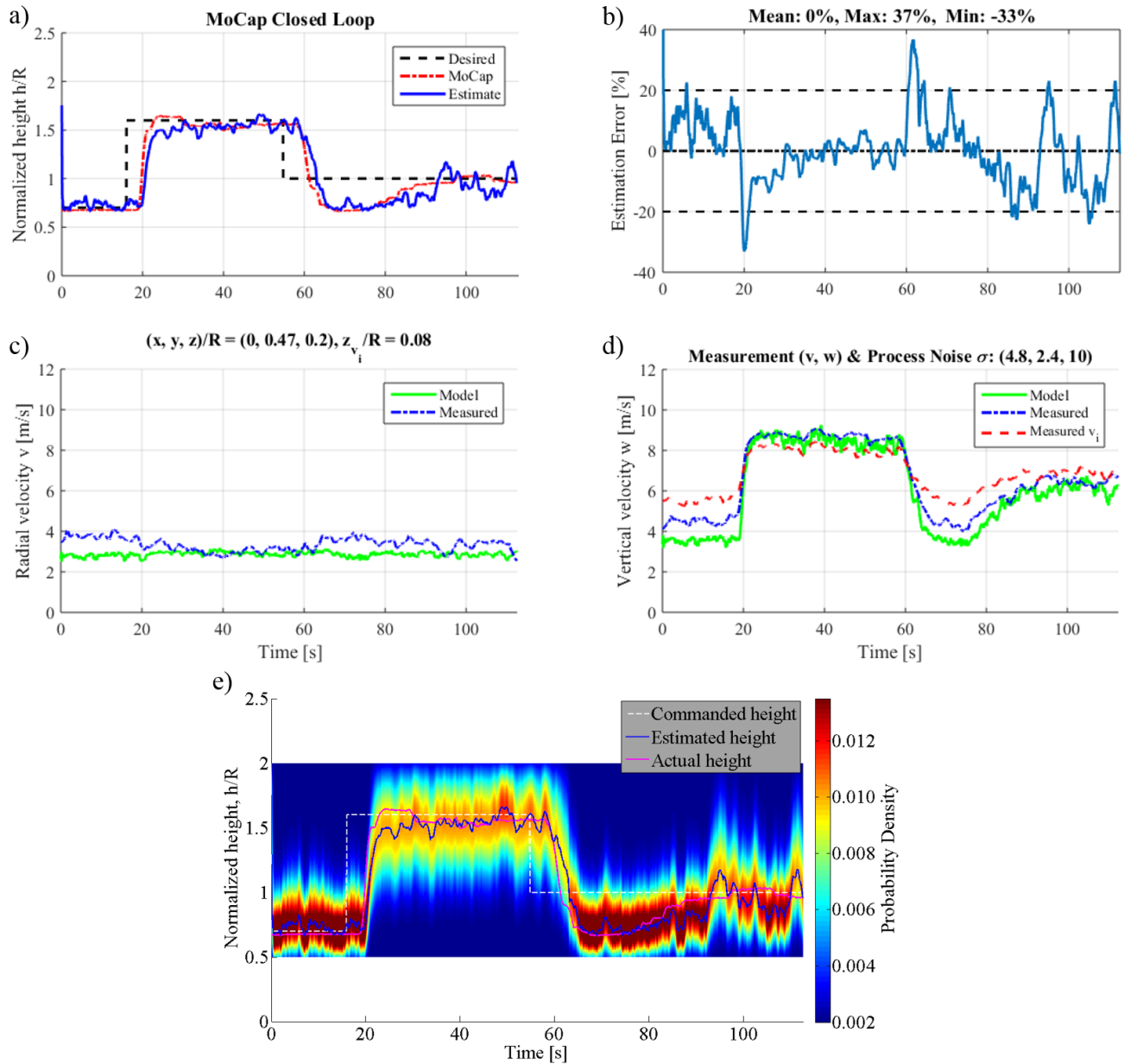


Fig. 13 Validation of Bayesian height estimation with closed-loop height tracking using motion capture. (a) Desired (dash), actual (dash-dot) and estimated (solid) normalized height h/R ; (b) percentage estimation error; (c) flow model (solid) and measured (dash-dot) radial velocity v ; (d) flow model (solid) and measured (dash-dot) vertical velocity w and measured induced velocity v_i (dash); (e) posterior PDF of height estimate.

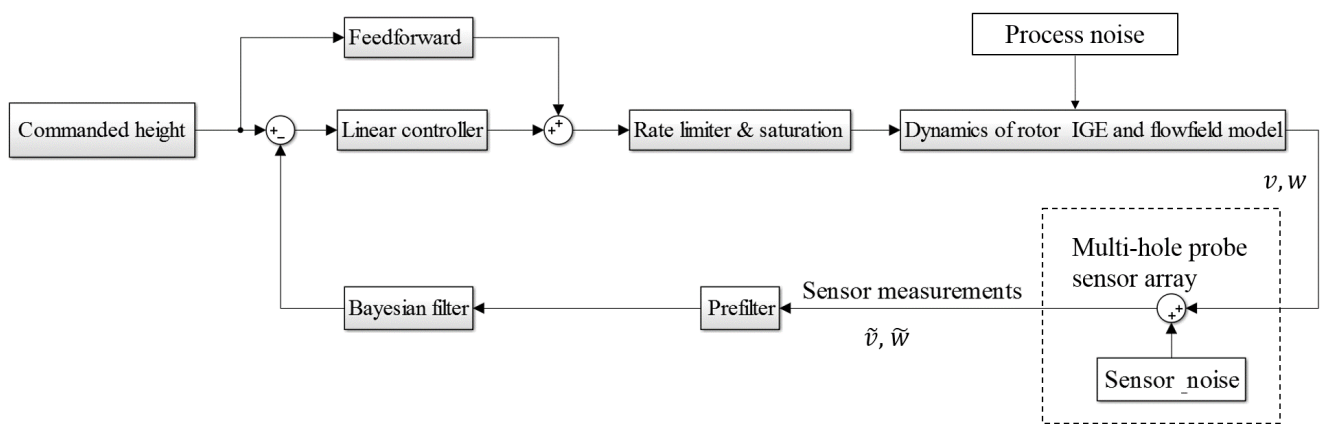


Fig. 14 Block diagram of Proportional-Integral feedback controller with feed-forward compensation.

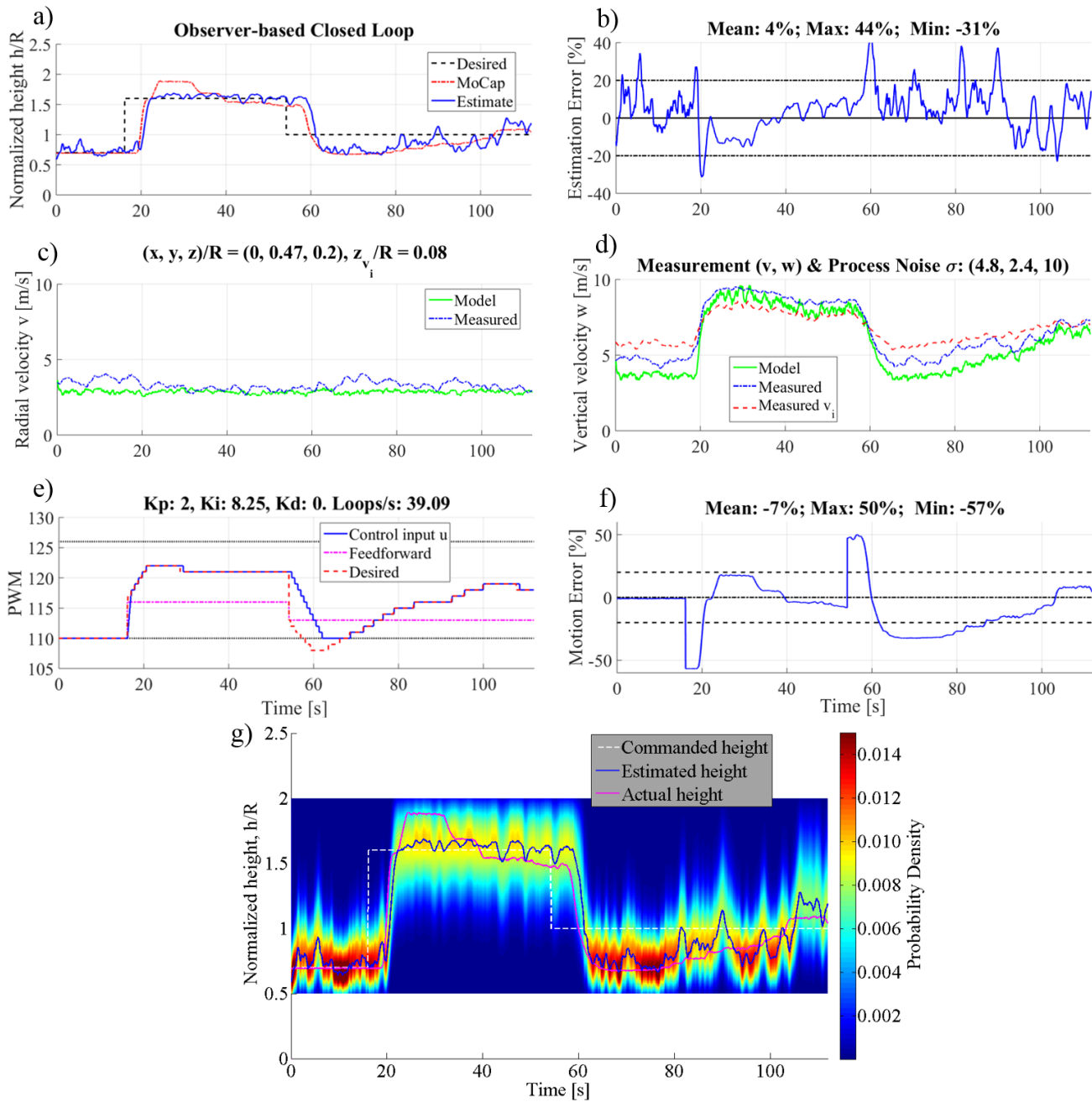


Fig. 15 Experimental validation of height-tracking framework using Bayesian height estimation and feedback-feed-forward control. (a) Desired (dash), ground truth (dash-dot) and estimated (solid) normalized height h/R ; (b) percentage estimation error; (c) flow model (solid) and measured (dash-dot) radial velocity v in m/s; (d) flow model (solid) and measured (dash-dot) vertical velocity w and measured induced velocity v_i (dashed) in m/s; (e) PWM control input v_2 (solid), feed-forward term (dash-dot), desired input (dash) prior to rate limiter and saturation. Loop speed of 39 loops/s; (f) percentage motion error; (g) posterior PDF of height estimate.

List of Figure Captions

- Fig. 1: Cheeseman and Bennett [14] potential flow model of rotor downwash in ground effect.
- Fig. 2: Schematic of ring-source potential-flow nomenclature.
- Fig. 3: Flowfield of ring-source potential flow evaluated at various heights, depicting streamlines and speed distributions; flow speed is $\|V\| = \sqrt{v^2 + w^2}$.
- Fig. 4: (a) Compound-pendulum heave test stand. (b) Free-body diagram of compound pendulum heave test stand.
- Fig. 5: (a) Free-body diagram of rotorcraft in ground effect. (b) Open-loop dynamics of rotorcraft in ground effect with constant input $\nu_1 = \nu_1^*$ and no damping. Initial conditions for height and velocity are 1.5m and 0.25m/s, respectively.
- Fig. 6: Comparison between measurements and quadratically smoothed values of velocity components.
- Fig. 7: Simulated closed-loop dynamics of rotorcraft in ground effect with no damping using the state feedback linear controller in Eqn. (38).
- Fig. 8: Simulations of the closed-loop system using the estimated height from the Bayesian filter. History of posterior PDF of normalized height h/R for (a) ascent maneuver from initial height and velocity of (0.7, 0/s), commanded height of 1.8, $(\sigma_p, \sigma_m) = (0.1, 0.15/s)$; (b) descent maneuver from initial height and velocity of (1.8, 0.2/s), commanded height of 0.6, $(\sigma_p, \sigma_m) = (0.08, 0.1/s)$. Estimated velocities with low-pass-filtered finite differencing for (a) and (b) are shown in (c) and (d).
- Fig. 9: (a) Block diagram for experimental instrumentation. (b) Heave test stand instrumentation with magnified view of two-pair differential pressure probe set providing radial and vertical velocity components.
- Fig. 10: Comparison between ring-source potential flow model in Eqns. (10), (11) and experimental results of radial v and vertical w velocity components for various radial locations. Error bars denote one standard deviation from the mean. Normalized height $h/R = 0.75$, normalized probe location $z/R = 0.18$, rotational speed $\omega = 2538$ RPM, induced velocity IGE $v_i = 4.34$ m/s.
- Fig. 11: (a) Probe placement in strong and weak ground effect. (b) Rotor side-view showing mid-radius

location with radial symmetry for two-pair flow probes (radial v and vertical w velocity components) and induced velocity v_i flow probe.

Fig. 12: Comparison between ring-source potential flow models (green) and experimental results (blue) of radial v , vertical w and induced v_i (red) velocity components for varying heights. Experiments were conducted on the heave test stand with probe vertical locations of $z/R = 0.10$ (solid circle), 0.20 (dashed diamond) and $z_{v_i} = 0.08$. The probes are radially symmetrical at (a)–(b) $(x, y) = (0, 0.47R)$; (c)–(d) $(x, y) = (0, 0.78R)$; (e)–(f) $(x, y) = (0, 0.87R)$.

Fig. 13: Validation of Bayesian height estimation with closed-loop height tracking using motion capture. (a) Desired (dash), actual (dash-dot) and estimated (solid) normalized height h/R ; (b) percentage estimation error; (c) flow model (solid) and measured (dash-dot) radial velocity v ; (d) flow model (solid) and measured (dash-dot) vertical velocity w and measured induced velocity v_i (dash); (e) posterior PDF of height estimate.

Fig. 14: Block diagram of Proportional-Integral feedback controller with feed-forward compensation.

Fig. 15: Experimental validation of height-tracking framework using Bayesian height estimation and feedback-feed-forward control. (a) Desired (dash), ground truth (dash-dot) and estimated (solid) normalized height h/R ; (b) percentage estimation error; (c) flow model (solid) and measured (dash-dot) radial velocity v in m/s; (d) flow model (solid) and measured (dash-dot) vertical velocity w and measured induced velocity v_i (dash) in m/s; (e) PWM control input ν_2 (solid), feed-forward term (dash-dot), desired input (dash) prior to rate limiter and saturation. Loop speed of 39 loops/s; (f) percentage motion error; (g) posterior PDF of height estimate.